Light-Induced Magnetic Fields for Neutral Atoms

Stefan Korenberg

3709302

Utrecht University

Supervision: P. van der Straten and R.A. Duine

June 23, 2013

Abstract

We explore light-induced magnetic fields for neutral atoms, which arise when atoms adiabatically follow spatially varying dressed states. We investigate normal modes resulting from phenomenological equations for atoms with different spin in a cigar shaped harmonic trap, in such magnetic fields and with spin drag present. Within the adiabatic approximation, we determine the light-induced magnetic field and we propose a setup to implement this in our experiment. Our results pave the way for studying transverse spin transport in the intrinsic regime.

Contents

Introduction

In recent years, a lot of research has been done in the field of ultra-cold atoms and it is still developing [1, 2, 3, 4]. Since the implementing of evaporative cooling after laser cooling, we can reach temperatures as low as nanokelvins, where a new form of matter was reached, Bose-Einstein condensates, and where we can study macroscopic quantum systems. Much research has been done towards spin-orbit coupling in these systems [5, 6, 7], and we will now address the spin Hall effect, where we have a force perpendicular to the speed of the atom, which depends on the spin of the atom. The spin Hall effect is widely studied in the field of spintronics as a means to get spin currents [8]. By studying the same effect in cold atom systems, we reach a completely different regime where the spin transport is determined by intrinsic effects, such as interactions, rather than extrinsic effects such as e.g. disorder.

For charged particles, the normal Hall effect arises when the particles move through a magnetic field, but for neutral atoms, this is not the case and we have no magnetic force perpendicular to their velocity. Here we will consider a pseudo magnetic field, induced by a properly designed laser field, which does couple to neutral particles and causes them to act like charged particles in a magnetic field, with the corresponding Lorentz force [9, 10]. It is a spin Hall effect, because it depends on the spin orientation of the particle. It arises when atoms adiabatically follow a spatially dependent dressed state, which is an eigenstate of the atom-light coupling. This magnetic field is a geometric effect, because it depends on the geometry of the path through the laser field, but not on the speed of the atom or the intensity of the laser. For the atoms to follow the local dressed state adiabatically, their speed cannot be too high, so that their position varies relatively slowly compared to their internal state. This is comparable to the Born-Oppenheimer approximation in molecular physics.

In this Bachelor Thesis, we explore these light-induced magnetic fields and how to implement them in our experiment. In order to get a feeling for what is happening and to get a first idea of the order of magnitude of the effects we could get, in section 1, we investigate normal modes of phenomenological equations for atoms with different spin, which are in a cigar shaped harmonic trap, with a magnetic field and spin drag. Here we describe the centre of mass motion by equations for a single particle. In section 2 we derive the expression for the pseudo magnetic field, starting with a standard Hamiltonian with an atom-light coupling term, and, after we apply the adiabatic approximation, ending up with a Hamiltonian which looks exactly the same as the Hamiltonian for a charged particle in a electromagnetic field, that gives rise to a Lorentz force. In section 3 we propose a laser configuration to implement this pseudo magnetic field in our experiment, and investigate the conditions that need to be satisfied and the choices in parameters we have. It turns out that we are able to choose our parameters such that we get a magnetic field which should give measurable effects. In section 4, we end with a discussion and an outlook on some possible measurements and other setups in order to increase the effect.

1 Phenomenological description

In this section we study the normal modes of the atomic cloud in the presence of a pseudo magnetic field on the basis of phenomenological equations.

1.1 Equations of motion

We start with phenomenological classical equations for the centre of mass, equations for a particle in a harmonic potential, with a magnetic field and linear spin-drag:

$$
\begin{aligned}
m_\uparrow \ddot{\vec{r}}_\uparrow &= -m_\uparrow \omega_i{}^2 \vec{r}_\uparrow &+&\quad \dot{\vec{r}}_\uparrow \times \vec{B} &-&\quad \gamma_i(\dot{\vec{r}}_\uparrow - \dot{\vec{r}}_\downarrow), \\
m_\downarrow \ddot{\vec{r}}_\downarrow &= -m_\downarrow \omega_i{}^2 \vec{r}_\downarrow &-&\quad \dot{\vec{r}}_\downarrow \times \vec{B} &-&\quad \gamma_i(\dot{\vec{r}}_\downarrow - \dot{\vec{r}}_\uparrow),
\end{aligned} \tag{1}
$$

where m is the mass, $\vec{r}_\sigma$ is the position of the centre of mass of the cloud with spin projection σ, ω_i is the trap-frequency in the i-direction, $\vec{B}$ is the (pseudo-) magnetic field and γ_i is the spin-drag in the i-direction. Here $i \in \{x, y, z\}$. We can have different ω and γ for different directions. Notice that the sign of the magnetic force is opposite for opposite spins. It turns out that linear spin-drag is a good approximation in our experiment [11].

Now we take $m_\uparrow = m_\downarrow \equiv m$, $\omega_x = \omega_y \equiv \omega_r$, $\gamma_x = \gamma_y \equiv \gamma_r$ and $\vec{B} = B\vec{y}$. We take $\vec{B}$ in the y-direction and not in the z-direction, because this is convenient in our experiment. Then we get, shown as a matrix equation:

$$
m \begin{pmatrix} \ddot{x}_\uparrow \\ \ddot{y}_\uparrow \\ \ddot{z}_\uparrow \\ \ddot{x}_\downarrow \\ \ddot{y}_\downarrow \\ \ddot{z}_\downarrow \end{pmatrix} = \begin{pmatrix} -\gamma_r & 0 & -B & \gamma_r & 0 & 0 \\ 0 & -\gamma_r & 0 & 0 & \gamma_r & 0 \\ B & 0 & -\gamma_z & 0 & 0 & \gamma_z \\ \gamma_r & 0 & 0 & -\gamma_r & 0 & B \\ 0 & \gamma_r & 0 & 0 & -\gamma_r & 0 \\ 0 & 0 & \gamma_z & -B & 0 & -\gamma_z \end{pmatrix} \cdot \begin{pmatrix} \dot{x}_\uparrow \\ \dot{y}_\uparrow \\ \dot{z}_\uparrow \\ \dot{x}_\downarrow \\ \dot{y}_\downarrow \\ \dot{z}_\downarrow \end{pmatrix}
$$

$$
+ \begin{pmatrix} -m\omega_r{}^2 & 0 & 0 & 0 & 0 & 0 \\ 0 & -m\omega_r{}^2 & 0 & 0 & 0 & 0 \\ 0 & 0 & -m\omega_z{}^2 & 0 & 0 & 0 \\ 0 & 0 & 0 & -m\omega_r{}^2 & 0 & 0 \\ 0 & 0 & 0 & 0 & -m\omega_r{}^2 & 0 \\ 0 & 0 & 0 & 0 & 0 & -m\omega_z{}^2 \end{pmatrix} \cdot \begin{pmatrix} x_\uparrow \\ y_\uparrow \\ z_\uparrow \\ x_\downarrow \\ y_\downarrow \\ z_\downarrow \end{pmatrix}. \tag{2}
$$

1.2 Dimensionless Equations

To make the equations dimensionless, we write $t = \tau t_0$ with t_0 a useful unit of time. Also we write $x = X r_0$, $y = Y r_0$ and $z = Z z_0$, with r_0 and z_0 useful units of distance. We use the same unit for the x- and y-direction, because these are equivalent. We take $t_0 = \frac{1}{\omega_r}$, which is $\frac{T_r}{2\pi}$, with T_r the radial oscillation period. Additionally we take $r_0 = \sqrt{\frac{k_\mathrm{B}T}{m\omega_r^2}}$ and $z_0 = \sqrt{\frac{k_\mathrm{B}T}{m\omega_z^2}}$, with k_B the Boltzmann

constant and T the temperature. This is about the maximum distance from the centre a particle with energy $k_\mathrm{B}T$ can classically reach in a harmonic potential.

With this the derivative with respect to time becomes $\frac{\partial}{\partial t} = \frac{\partial \tau}{\partial t}\frac{\partial}{\partial \tau} = \frac{1}{t_0}\frac{\partial}{\partial \tau} = \omega_r \frac{\partial}{\partial \tau}$ and thus we can rewrite the derivatives with respect to time as $\dot{x}_\uparrow = r_0 \omega_r \frac{\partial X_\uparrow}{\partial \tau}, \dot{z}_\uparrow = z_0 \omega_r \frac{\partial Z_\uparrow}{\partial \tau}, \ddot{x}_\uparrow = r_0 \omega_r^2 \frac{\partial^2 X_\uparrow}{\partial \tau^2}$ and $\ddot{z}_\uparrow = z_0 \omega_r^2 \frac{\partial^2 Z_\uparrow}{\partial \tau^2}$. Using $\frac{r_0}{z_0} = \frac{\sqrt{\frac{k_\mathrm{B}T}{m\omega_r^2}}}{\sqrt{\frac{k_\mathrm{B}T}{m\omega_z^2}}} = \frac{\omega_z}{\omega_r}$, the dimensionless equations then become:

$$\begin{pmatrix}\ddot{X}_\uparrow\\ \ddot{Y}_\uparrow\\ \ddot{Z}_\uparrow\\ \ddot{X}_\downarrow\\ \ddot{Y}_\downarrow\\ \ddot{Z}_\downarrow\end{pmatrix} = \frac{1}{m\omega_r}\begin{pmatrix}-\gamma_r & 0 & -B\frac{\omega_r}{\omega_z} & \gamma_r & 0 & 0\\ 0 & -\gamma_r & 0 & 0 & \gamma_r & 0\\ B\frac{\omega_z}{\omega_r} & 0 & -\gamma_z & 0 & 0 & \gamma_z\\ \gamma_r & 0 & 0 & -\gamma_r & 0 & B\frac{\omega_r}{\omega_z}\\ 0 & \gamma_r & 0 & 0 & -\gamma_r & 0\\ 0 & 0 & \gamma_z & -B\frac{\omega_z}{\omega_r} & 0 & -\gamma_z\end{pmatrix}\cdot\begin{pmatrix}\dot{X}_\uparrow\\ \dot{Y}_\uparrow\\ \dot{Z}_\uparrow\\ \dot{X}_\downarrow\\ \dot{Y}_\downarrow\\ \dot{Z}_\downarrow\end{pmatrix}$$

$$+\begin{pmatrix}-1 & 0 & 0 & 0 & 0 & 0\\ 0 & -1 & 0 & 0 & 0 & 0\\ 0 & 0 & -(\frac{\omega_z}{\omega_r})^2 & 0 & 0 & 0\\ 0 & 0 & 0 & -1 & 0 & 0\\ 0 & 0 & 0 & 0 & -1 & 0\\ 0 & 0 & 0 & 0 & 0 & -(\frac{\omega_z}{\omega_r})^2\end{pmatrix}\cdot\begin{pmatrix}X_\uparrow\\ Y_\uparrow\\ Z_\uparrow\\ X_\downarrow\\ Y_\downarrow\\ Z_\downarrow\end{pmatrix}. \quad (3)$$

Now we choose to use the following parameters: $a = \frac{\gamma_r}{\gamma_z}$, $b = \frac{B}{\gamma_z}$ and $c = \frac{\gamma_z}{m}$, where a and b are dimensionless, while c is not. These parameters are chosen this way to see the competition between B and γ_z. We do not make c dimensionless in order to keep c and ω_r independent parameters.
In equation 3, the y-direction is completely uncoupled, with two normal modes in this direction; an in-phase harmonic oscillation and an out-of-phase damped harmonic oscillation. The equations for the x- and z-direction are, with the new parameters:

$$\begin{pmatrix}\ddot{X}_\uparrow\\ \ddot{Z}_\uparrow\\ \ddot{X}_\downarrow\\ \ddot{Z}_\downarrow\end{pmatrix} = \frac{c}{\omega_r}\begin{pmatrix}-a & -b\frac{\omega_r}{\omega_z} & a & 0\\ b\frac{\omega_z}{\omega_r} & -1 & 0 & 1\\ a & 0 & -a & b\frac{\omega_r}{\omega_z}\\ 0 & 1 & -b\frac{\omega_z}{\omega_r} & -1\end{pmatrix}\begin{pmatrix}\dot{X}_\uparrow\\ \dot{Z}_\uparrow\\ \dot{X}_\downarrow\\ \dot{Z}_\downarrow\end{pmatrix} + \begin{pmatrix}-1 & 0 & 0 & 0\\ 0 & -(\frac{\omega_z}{\omega_r})^2 & 0 & 0\\ 0 & 0 & -1 & 0\\ 0 & 0 & 0 & -(\frac{\omega_z}{\omega_r})^2\end{pmatrix}\begin{pmatrix}X_\uparrow\\ Z_\uparrow\\ X_\downarrow\\ Z_\downarrow\end{pmatrix}.$$

$$(4)$$

1.3 Normal modes

To determine the normal modes, we try a solution of the form $\vec{a} \cdot e^{i\omega\tau}$. The vector $\vec{a}$ is a vector with components for both spins, like in the matrix equations. Equation 4 puts restrictions on $\vec{a}$ and ω, and in order to satisfy this, the following equation has to hold:

$$-\omega^2 M_a \cdot \vec{a} = i\omega M_v \cdot \vec{a} + M_r \cdot \vec{a}, \tag{5}$$

where M_a, M_v and M_r are the matrices in front of the acceleration-, velocity- and positionvector. Rewritten this becomes:

$$(-\omega^2 M_a - i\omega M_v - M_r) \cdot \vec{a} = \vec{0}. \tag{6}$$

To find non-trivial solutions for $\vec{a}$, the determinant of the combined matrix on the left side has to be equal to zero. This gives an equation for ω and by this the possible frequencies of the normal modes are determined. When we substitute every possible ω, we find the corresponding $\vec{a}$.

In the case of the dimensionless equations from equation 4, this gives the following equation for ω:

$$\det \begin{pmatrix} -\omega^2 + \frac{aci\omega}{\omega_r} + 1 & \frac{ibc\omega}{\omega_z} & -\frac{iac\omega}{\omega_r} & 0 \\ -\frac{ibc\omega\omega_z}{\omega_r^2} & -\omega^2 + \frac{ci\omega}{\omega_r} + \frac{\omega_z^2}{\omega_r^2} & 0 & -\frac{ic\omega}{\omega_r} \\ -\frac{iac\omega}{\omega_r} & 0 & -\omega^2 + \frac{aci\omega}{\omega_r} + 1 & -\frac{ibc\omega}{\omega_z} \\ 0 & -\frac{ic\omega}{\omega_r} & \frac{ibc\omega\omega_z}{\omega_r^2} & -\omega^2 + \frac{ci\omega}{\omega_r} + \frac{\omega_z^2}{\omega_r^2} \end{pmatrix} = 0. \tag{7}$$

For a spherical trap, everything simplifies a lot, but for an asymmetric trap this is not the case. In most cases, it is still possible to find the ω analytically, but the expressions are quite large and give little insight. Also Mathematica is not able to solve for $\vec{a}$ and therefore I have chosen to determine these numerically, since it does not give many advantages to try to get these analytically.
The determinant is a polynomial of degree 8 in ω and thus the equation has 8 solutions for ω. These give 4 qualitatively different motions. The found ω are expressed in dimensionless units; t_0 is merged into the used ω to make it dimensionless. So what is really determined, is, in normal units, $\omega t_0 = \frac{\omega}{\omega_r}$.

In appendix A, the normal modes are examined in detail. Here, we will focus on the normal mode which starts from the in-phase oscillation in the z-direction, because this one is the most relevant for our experiment. To make the figures, we used the following values: $c = 1\,\mathrm{Hz}$, $\omega_r = 100\,\frac{\mathrm{rad}}{\mathrm{s}}$, $\omega_z = 4\,\frac{\mathrm{rad}}{\mathrm{s}}$ and $a = 0$. We choose c this way, because c only comes in pairs with b in this mode, since there is no drag. Another way of looking at this is that we choose a new parameter $bc = \frac{B}{m}$ for modes without drag. We choose the ω this way, because they are relevant for our experiment. We choose a this way, because we are not hydrodynamic in the radial direction.

1.4 In-phase oscillation in the z-direction

This mode starts from the mode in which both clouds oscillate in-phase in the z-direction. When we turn on the B-field, the clouds are separated in the r-direction, since the B-field acts oppositely on the clouds and their velocities are (approximately) in the same direction. Since there is no relative movement in the z-direction and there is no drag in the r-direction, there is no damping in this mode. In figure 1 the angular frequency is plotted against the B-field and in figure 2 the trajectory is plotted for $\frac{B}{m} = 100\,\mathrm{Hz}$.
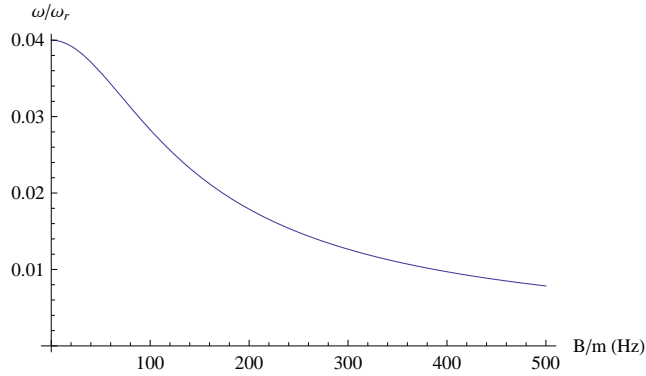

Figure 1: The angular frequency $\frac{\omega}{\omega_r}$ as a function of $\frac{B}{m}$ for the in-phase oscillation in the z-direction. Because there is no damping this quantity is completely real.
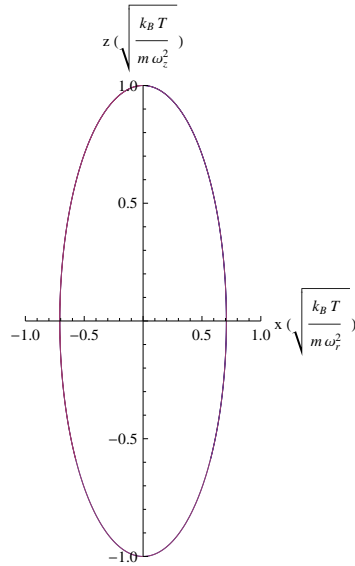

Figure 2: Trajectory of the normal mode starting from the in-phase oscillation in the z-direction. Note that we use different units on the axes. Here, $b = 100$, so $\frac{B}{m} = 100\,\mathrm{Hz}$.

1.5 Numerical solutions

This section is about numerical solutions of the equations with proper initial conditions. The most relevant initial conditions are with both clouds given an initial displacement in the z-direction and no initial velocity. We will only state the results for this case. By applying a real magnetic field with a gradient, as a potential, we can give the clouds a displacement. Because the spins of the clouds are opposite, they get an opposite displacement. In this setup, we thus (approximately) start in the out-of-phase oscillation, the spin dipole mode, for which the trajectory is shown in figure 3.
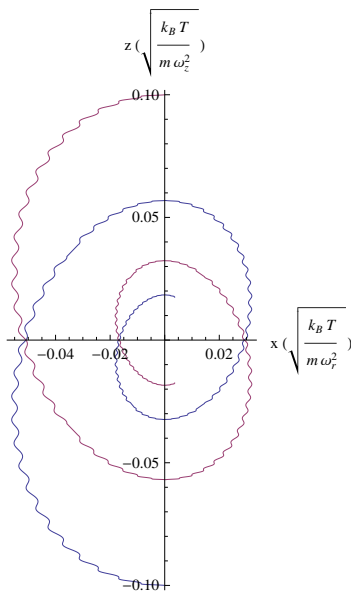

Figure 3: Numerically calculated trajectory in which the clouds start with an opposite displacement. Note that we use different units on the axes. Here, $b = 100$ and $c = 1\,\text{Hz}$, so $\frac{B}{m} = bc = 100\,\text{Hz}$.

However, drag is very important in this mode, and therefore it is better to give both clouds the same displacement instead of opposite. This can be realized by first giving one cloud a displacement, then flipping half of the spins, creating two clouds and immediately after that letting them go. This way we have two clouds with different spin, that start with the same displacement. Another way of getting this initial situation is to displace the minimum of the trap. When done fast enough, this is effectively the same as giving our clouds a displacement. We choose our parameters the same as before, for the same reasons: $a = 0$, $c = 1\,\text{Hz}$, $\omega_r = 100\,\frac{\text{rad}}{\text{s}}$ and $\omega_z = 4\,\frac{\text{rad}}{\text{s}}$. Figure 4 and figure 5 show the trajectories for these initial conditions and parameters and different values of b.
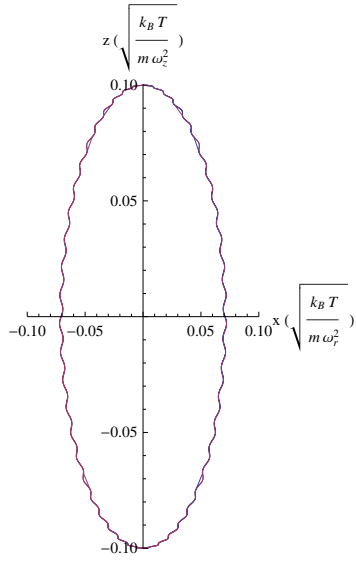
Figure 4: Numerically calculated trajectory in which the clouds start with the same displacement. Note that we use different units on the axes. Here, $b = 100$ and $c = 1\,\text{Hz}$, so $\frac{B}{m} = bc = 100\,\text{Hz}$.
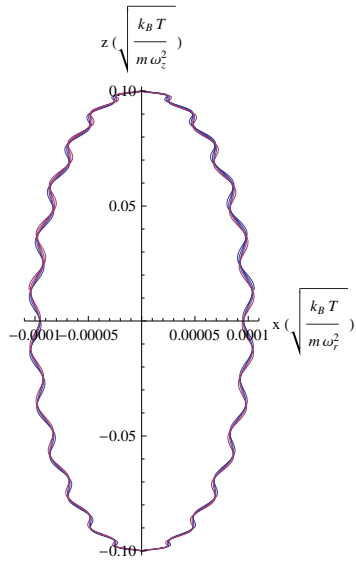

Figure 5: Numerically calculated trajectory in which the clouds start with the same displacement. Note that we use different units on the axes. Here, $b = 0.1$ and $c = 1\,\text{Hz}$, so $\frac{B}{m} = bc = 0.1\,\text{Hz}$.

From the figures, we see that the trajectories are similar, even though b differs by a factor 10^3. The differences for different b are the amplitude in the r-direction, which gets larger with larger b, and the behaviour of the wiggles. Also we see that there is indeed no damping ($a = 0$ and no relative motion in the z-direction). The observation that the trajectories are similar has to do with the shape of the trap, a cigar shape. Because of that the speed in the r-direction remains relatively small and the B-field has a small effect on the movement in the z-direction. For the r-direction, it gives rise to a force which is proportional to the speed in the z-direction. This varies relatively slowly and because of that it can be seen as a constant displacement of the minimum of the trap in the r-direction. The force in the r-direction is opposite for the two clouds, the displacement is thus also opposite and the clouds separate. Above arguments are only valid because of the shape of the trap and in this case the B-field, in first approximation, only affects the displacement of the clouds in the r-direction.

On $z = 0$, the clouds have the highest speed in the z-direction and therefore also the largest displacement. Moreover, it is the most natural point to look at in the experiment. In figure 6 the displacement in the r-direction at $z = 0$ is plotted as a function of $\frac{B}{m}$, as determined by numerical calculations, together with values for the normal mode and an analytic expression which is given in the next subsection.
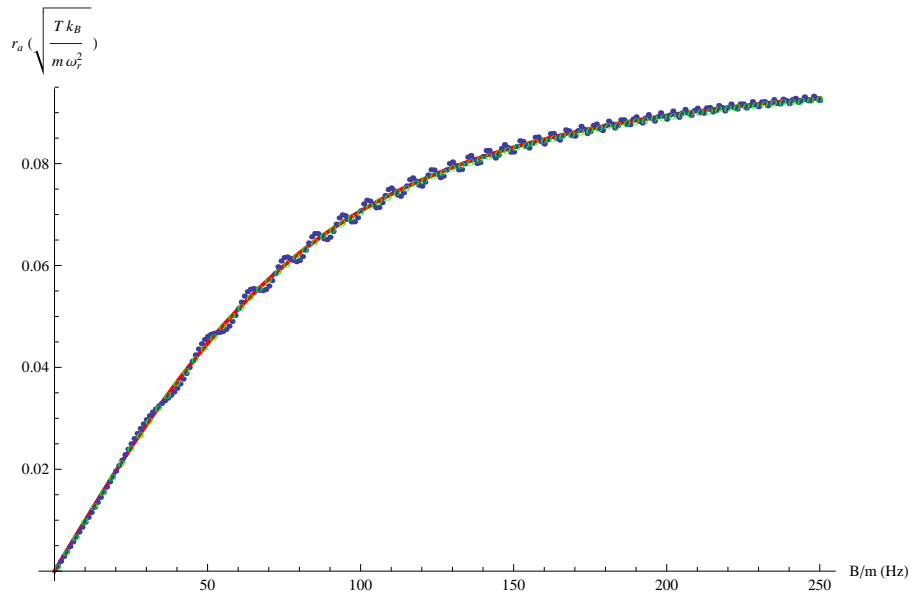

Figure 6: The radial displacement at $z = 0$ as a function of $\frac{B}{m}$ (blue) plotted together with our analytic expression (red line) and values found for the normal mode (green).

1.5.1 Approximation for the displacement

With the above observations about the behaviour in a cigar shaped trap, we derive an analytic expression as an approximation for the displacement. This expression follows from classical energy considerations. At the initial situation the total energy is equal to $\frac{1}{2}m\omega_z^2 z_{\text{start}}^2$ and this is conserved because there is no drag. Here z_{start} is the starting amplitude. At $z = 0$, there is no potential energy for the z-direction and the energy is equal to $\frac{1}{2}mv_z^2 + \frac{1}{2}m\omega_r^2 r_a^2$, neglecting the speed in the r-direction. Here, v_z is the speed in the z-direction and r_a is the amplitude in the r-direction. The B-field gives a force in the r-direction equal to $v_z B$ and this is (approximately) compensated by the force of the harmonic potential in the r-direction as a result of the displacement in the r-direction. This way we look at it as a displacement of the equilibrium point in the r-direction. The force of the harmonic potential in the r-direction is equal to $m\omega_r^2 r_a$ and with this we get the following equations:

$$\frac{1}{2}m\omega_z^2 z_{\text{start}}^2 = \frac{1}{2}mv_z^2 + \frac{1}{2}m\omega_r^2 r_a^2, \tag{8}$$

$$v_z B = m\omega_r^2 r_a. \tag{9}$$

We can eliminate v_z and rewrite the resulting equation to get an expression for r_a:

$$r_a = \frac{B\omega_z z_{\text{start}}}{\omega_r \sqrt{m^2\omega_r^2 + B^2}}, \tag{10}$$

and this can be rewritten in terms of our used parameters

$$r_a = \frac{bc\omega_z z_{\text{start}}}{\omega_r \sqrt{\omega_r^2 + b^2 c^2}}. \tag{11}$$

In our numerical calculations z_{start} and r_a are given in units of z_0 and r_0. To get our analytic expression in these units, we need to substitute $z_{\text{start}} \rightarrow \bar{z}_{\text{start}} z_0$ and $r_a \rightarrow \bar{r}_a r_0$. This way we get a factor $\frac{z_0}{r_0} = \frac{\omega_r}{\omega_z}$ in our expression and with this we get for the analytic expression in new units:

$$\bar{r}_a = \frac{bc\bar{z}_{\text{start}}}{\sqrt{\omega_r^2 + b^2 c^2}}. \tag{12}$$

When we plot this together with the found numerical values, we get figure 6, which shows that our expression is a good first approximation. The values found for the in-phase normal mode in the z-direction are also plotted, which fit even better.

1.5.2 Numerical ω

The trajectory starts in a maximum in the z-direction and when the trajectory is at the maximum again, the movement repeats itself. Therefore we can numerically determine the period by looking at the maxima. We can then determine ω by $\omega = \frac{2\pi}{T_z}$, with T_z the period. The result of this calculation for different b is shown in figure 7. The parameters are again chosen to be $a = 0$, $\omega_r = 100 \frac{\text{rad}}{\text{s}}$ and $\omega_z = 4 \frac{\text{rad}}{\text{s}}$.
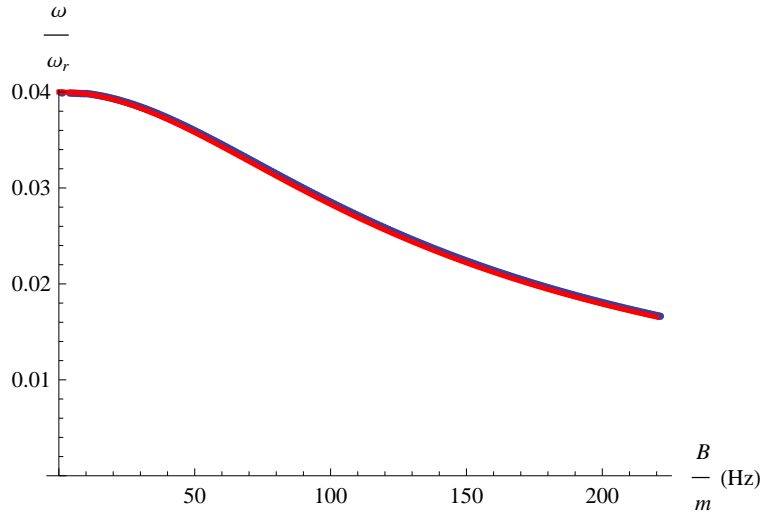

Figure 7: Numerically determined ω as a function of $\frac{B}{m}$ with the initial condition that both clouds have the same displacement of $0.1 z_0$ (blue), plotted together with ω from the in-phase normal mode of the z-direction (red line).

Because we start in the in-phase normal mode in the z-direction, when the magnetic field is absent, thus without any coupling to the r-direction, we start with $\omega = 0.04\omega_r = \omega_z$, in normal real units. When we turn on the B-field, we do not exactly start in this normal mode anymore, because in the normal mode the speed in the r-direction is nonzero at the maximum of the z-direction, while in our initial conditions it is. As a result of this we get the wiggles in the trajectories of figure 4 and figure 5 compared to the clean ellipse of the normal mode in figure 2. However, we do excite this normal mode most and because of that ω as a function of b is almost the same as is shown in figure 7.

2 Derivation of the pseudo magnetic field

This section is about the origin of the pseudo magnetic field. We closely follow the articles of Dalibard *et al.*[9] and Zhu *et al.*[10]. The most important assumption is that the atoms adiabatically follow a spatially dependent dressed state in the light field. From this we get a Hamiltonian which has exactly the same form as the Hamiltonian of an atom in an electromagnetic field, which gives rise to an effective magnetic field when the rotation of the pseudo vector potential $\vec{A}$ is nonzero. The adiabatic assumption will be valid when the local dressed state varies much more slowly than the internal state of the atom. Therefore the speed of the atoms cannot be too high, because this determines the speed of change in the local dressed state. This is captured in an adiabatic condition.

We begin with the following Hamiltonian:

$$\hat{H} = \left[\frac{\hat{P}^2}{2m} + V(\vec{r}) \right] \hat{I} + \hbar \hat{U}, \tag{13}$$

where $\hat{P}$ is the momentum operator, m is the mass, $V(\vec{r})$ is the potential, $\hbar$ is the Planck constant and $\hat{U}$ is the atom light coupling, given by

$$\hat{U} = \begin{pmatrix} 0 & 0 & \Omega_1 \\ 0 & 0 & \Omega_2 \\ \Omega_1^* & \Omega_2^* & 2\Delta \end{pmatrix}, \tag{14}$$

where Ω_i are the Rabi frequencies and Δ is the detuning of the laser light from resonance. This is appropriate for a Λ-type atom, represented in figure 8, which has an excited state and two different ground states. $\hat{U}$ is given in the internal basis as shown in figure 8 and we are now going to change basis into the eigenstates of the atom light coupling.
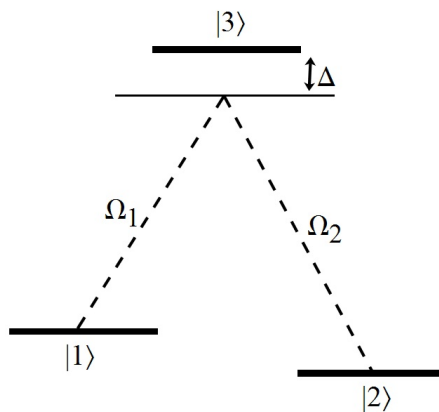

Figure 8: Λ-type atom with two ground states and one excited state, coupled by Rabi frequencies Ω_1 and Ω_2, with detuning Δ from resonance.

2.1 Eigenstates

First we write $\Omega_1 = \Omega \sin(\theta)e^{i\phi}$ and $\Omega_2 = \Omega \cos(\theta)$, where $\Omega = \sqrt{|\Omega_1|^2 + |\Omega_2|^2}$. The eigenstates of $\hat{U}$ are our dressed states and we will choose these as our new internal basis, for which we are going to write down the new expression of the Hamiltonian. The eigenstates are the following [10]:

$$|\chi_1\rangle = \begin{pmatrix} \cos(\theta) \\ -\sin(\theta)e^{-i\phi} \\ 0 \end{pmatrix}, \tag{15}$$

with eigenvalue 0.

$$|\chi_2\rangle = \begin{pmatrix} \sin(\theta)\cos(\gamma)e^{i\phi} \\ \cos(\theta)\cos(\gamma) \\ -\sin(\gamma) \end{pmatrix}, \tag{16}$$

with eigenvalue $\Delta - \sqrt{\Delta^2 + \Omega^2}$, where γ is defined by $\tan \gamma = \frac{\sqrt{\Delta^2 + \Omega^2} - \Delta}{\Omega}$.

$$|\chi_3\rangle = \begin{pmatrix} \sin(\theta)\sin(\gamma)e^{i\phi} \\ \cos(\theta)\sin(\gamma) \\ \cos(\gamma) \end{pmatrix}, \tag{17}$$

with eigenvalue $\Delta + \sqrt{\Delta^2 + \Omega^2}$.

In appendix B we show that these states are indeed eigenstates with the corresponding eigenvalues. It is easily shown that they are normalized, $||\chi_i\rangle| = 1$. Also they are mutually orthogonal, as they should be for a Hermitian matrix, so it is an orthonormal basis:

$$\langle \chi_2 | \chi_3 \rangle = \sin^2(\theta)\sin(\gamma)\cos(\gamma) + \cos^2(\theta)\sin(\gamma)\cos(\gamma) - \sin(\gamma)\cos(\gamma) = 0,$$
$$\langle \chi_2 | \chi_1 \rangle = \cos(\theta)\sin(\theta)\cos(\gamma)e^{-i\phi} - \sin(\theta)e^{-i\phi}\cos(\theta)\cos(\gamma) = 0,$$
$$\langle \chi_3 | \chi_1 \rangle = \cos(\theta)\sin(\theta)\sin(\gamma)e^{-i\phi} - \sin(\theta)e^{-i\phi}\cos(\theta)\sin(\gamma) = 0. \tag{18}$$

2.2 Momentum operator

Now we calculate how the momentum operator $\hat{P}$ acts on the full atomic state, when written in the dressed internal basis, which is also spatially dependent.

$$\hat{P}\left|\Psi\right\rangle = -i\hbar\vec{\nabla}\sum_{j=1}^{3}\psi_j(\vec{r},t)\left|\chi_j(\vec{r})\right\rangle$$

$$= -i\hbar\sum_{j=1}^{3}((\vec{\nabla}\psi_j(\vec{r},t))\left|\chi_j(\vec{r})\right\rangle + \psi_j(\vec{r},t)\left|\vec{\nabla}\chi_j(\vec{r})\right\rangle)$$

$$= -i\hbar\sum_{j,l=1}^{3}((\delta_{lj}\vec{\nabla}\psi_l)\left|\chi_j\right\rangle + \left\langle\chi_l|\vec{\nabla}\chi_j\right\rangle\psi_j\left|\chi_l\right\rangle)$$

$$= -i\hbar\sum_{j,l=1}^{3}(\delta_{lj}\vec{\nabla}\psi_l + \left\langle\chi_j|\vec{\nabla}\chi_l\right\rangle\psi_l)\left|\chi_j\right\rangle$$

$$= \sum_{j,l=1}^{3}((\delta_{lj}\hat{P} - \vec{A}_{jl})\psi_l)\left|\chi_j\right\rangle , \tag{19}$$

where we defined $\vec{A}_{jl} = i\hbar\left\langle\chi_j|\vec{\nabla}\chi_l\right\rangle$ and we used the completeness relation in the third step. Notice that we have re-expressed the operator in a way that only acts on the spatial state of the atom. When written as a matrix this equation becomes:

$$\hat{P}\left|\Psi\right\rangle = \begin{pmatrix} \hat{P}-\vec{A}_{11} & -\vec{A}_{12} & -\vec{A}_{13} \\ -\vec{A}_{21} & \hat{P}-\vec{A}_{22} & -\vec{A}_{23} \\ -\vec{A}_{31} & -\vec{A}_{32} & \hat{P}-\vec{A}_{33} \end{pmatrix}\cdot\begin{pmatrix} \psi_1 \\ \psi_2 \\ \psi_3 \end{pmatrix}, \tag{20}$$

where $\left|\Psi\right\rangle = (\psi_1,\psi_2,\psi_3)^T$ is in the new internal basis of dressed states of the atom light coupling. With this we find for $\hat{P}^2$:

$$\hat{P}^2\left|\Psi\right\rangle = \begin{pmatrix} \hat{P}-\vec{A}_{11} & -\vec{A}_{12} & -\vec{A}_{13} \\ -\vec{A}_{21} & \hat{P}-\vec{A}_{22} & -\vec{A}_{23} \\ -\vec{A}_{31} & -\vec{A}_{32} & \hat{P}-\vec{A}_{33} \end{pmatrix}\cdot\begin{pmatrix} \hat{P}-\vec{A}_{11} & -\vec{A}_{12} & -\vec{A}_{13} \\ -\vec{A}_{21} & \hat{P}-\vec{A}_{22} & -\vec{A}_{23} \\ -\vec{A}_{31} & -\vec{A}_{32} & \hat{P}-\vec{A}_{33} \end{pmatrix}\begin{pmatrix} \psi_1 \\ \psi_2 \\ \psi_3 \end{pmatrix} =$$

$$\begin{pmatrix} \left(\hat{P}-\vec{A}_{11}\right)^2+\vec{A}_{12}\vec{A}_{21}+\vec{A}_{13}\vec{A}_{31} & -\vec{A}_{12}\left(\hat{P}-\vec{A}_{22}\right)-\left(\hat{P}-\vec{A}_{11}\right)\vec{A}_{12}+\vec{A}_{13}\vec{A}_{32} & -\vec{A}_{13}\left(\hat{P}-\vec{A}_{33}\right)-\left(\hat{P}-\vec{A}_{11}\right)\vec{A}_{13}+\vec{A}_{12}\vec{A}_{23} \\ -\vec{A}_{21}\left(\hat{P}-\vec{A}_{11}\right)-\left(\hat{P}-\vec{A}_{22}\right)\vec{A}_{21}+\vec{A}_{23}\vec{A}_{31} & \left(\hat{P}-\vec{A}_{22}\right)^2+\vec{A}_{12}\vec{A}_{21}+\vec{A}_{23}\vec{A}_{32} & \vec{A}_{13}\vec{A}_{21}-\left(\hat{P}-\vec{A}_{22}\right)\vec{A}_{23}-\vec{A}_{23}\left(\hat{P}-\vec{A}_{33}\right) \\ -\vec{A}_{31}\left(\hat{P}-\vec{A}_{11}\right)+\vec{A}_{21}\vec{A}_{32}-\left(\hat{P}-\vec{A}_{33}\right)\vec{A}_{31} & -\vec{A}_{32}\left(\hat{P}-\vec{A}_{22}\right)+\vec{A}_{12}\vec{A}_{31}-\left(\hat{P}-\vec{A}_{33}\right)\vec{A}_{32} & \left(\hat{P}-\vec{A}_{33}\right)^2+\vec{A}_{13}\vec{A}_{31}+\vec{A}_{23}\vec{A}_{32} \end{pmatrix}\begin{pmatrix} \psi_1 \\ \psi_2 \\ \psi_3 \end{pmatrix}.$$

$$\tag{21}$$

In our adiabatic approach, we assume the off-diagonal elements of the Hamiltonian negligible compared to the diagonal. If that would not be the case and we start in one particular dressed state, the coupling between the different dressed states would, according to the Schrödinger equation, give a nonzero time derivative of another dressed state, while we assume that the atom stays in the dressed state we started in. The condition for this is given in the next section in equation 35. For now we just state what it looks like when we apply the adiabatic approximation. For $\hat{P}^2$ we have found for the diagonal elements, $\hat{P}^2_{ll} = (\hat{P} - \vec{A}_{ll})^2 + \sum_{j \neq l} \vec{A}_{lj}\vec{A}_{jl}$ and with this the diagonal elements of our new Hamiltonian (in the basis of dressed states) become

$$\hat{H}_{ll} = \frac{1}{2m}\left((\hat{P} - \vec{A}_{ll})^2 + \sum_{j \neq l} \vec{A}_{lj}\vec{A}_{jl}\right) + V + \hbar\lambda_l = \frac{(\hat{P} - \vec{A}_{ll})^2}{2m} + V^*, \quad (22)$$

where $V^* = \sum_{j \neq l} \frac{\vec{A}_{lj}\vec{A}_{jl}}{2m} + V + \hbar\lambda_l$, the effective potential and λ_l is the eigenvalue $\hat{U}$, which arises because we are in a basis of eigenstates. In appendix C, V^* is worked out more explicitly and there will also be a notion about where the adiabatic condition comes from.

2.2.1 Schrödinger equation

By projecting the full Schrödinger equation on $|\chi_l\rangle$, taking the inner product with $\langle\chi_l|$, we find:

$$i\hbar\frac{\partial}{\partial t}\psi_l = \hat{H}_{ll}\psi_l = \left(\frac{(\hat{P} - \vec{A}_{ll})^2}{2m} + V^*\right)\psi_l. \quad (23)$$

Here we used the result for the Hamiltonian, that it only has diagonal elements and that the eigenstates are independent of time, so that $\langle\chi_l| i\hbar\frac{\partial}{\partial t}(\psi_l |\chi_l\rangle) = i\hbar\frac{\partial}{\partial t}\psi_l$.

We see that this has the same form as the Schrödinger equation for a charged particle in an electromagnetic field, for which the Hamiltonian looks like $\hat{H} = \frac{(\hat{P} - q\vec{A})^2}{2m} + qV$. This gives rise to the Lorentz force, in particular to a magnetic force when the rotation of $\vec{A}$ is nonzero. Here q is the charge and to get our Hamiltonian, we take $q = 1$. Since we have the same Schrödinger equation, we have the same motion and therefore we can indeed identify $\vec{A}_{ll}$ with the vector potential in electrodynamics, with the same properties with respect to the motion of the particles, in particular that it gives rise to a magnetic field equal to the rotation of this vector potential. In this case, $\vec{A}_{ll}$ does not depend on time, we do not get a pseudo electric field from the vector potential.

2.3 Effective magnetic field

Now we calculate explicitly what the effective vector potential and the effective magnetic field look like. First we calculate:

$$\frac{\partial}{\partial x}\left|\chi_1\right\rangle = \frac{\partial}{\partial x}\begin{pmatrix}\cos(\theta) \\ -\sin(\theta)e^{-i\phi} \\ 0\end{pmatrix} = \begin{pmatrix}-\sin(\theta)\frac{\partial\theta}{\partial x} \\ i\sin(\theta)e^{-i\phi}\frac{\partial\phi}{\partial x} - \cos(\theta)e^{-i\phi}\frac{\partial\theta}{\partial x} \\ 0\end{pmatrix},$$

and similar for $\frac{\partial}{\partial y}$ and $\frac{\partial}{\partial z}$. With this we have for the vector potential

$$\begin{aligned}\vec{A}_{11} &= i\hbar\left\langle\chi_1|\vec{\nabla}\chi_1\right\rangle \\ &= i\hbar\begin{pmatrix}-i\frac{\partial\phi}{\partial x}\sin^2(\theta) + \cos(\theta)\frac{\partial\theta}{\partial x}\sin(\theta) - \cos(\theta)\frac{\partial\theta}{\partial x}\sin(\theta) \\ -i\frac{\partial\phi}{\partial y}\sin^2(\theta) + \cos(\theta)\frac{\partial\theta}{\partial y}\sin(\theta) - \cos(\theta)\frac{\partial\theta}{\partial y}\sin(\theta) \\ -i\frac{\partial\phi}{\partial z}\sin^2(\theta) + \cos(\theta)\frac{\partial\theta}{\partial z}\sin(\theta) - \cos(\theta)\frac{\partial\theta}{\partial z}\sin(\theta)\end{pmatrix} \\ &= \hbar\sin^2(\theta)\vec{\nabla}\phi.\end{aligned}\tag{24}$$

For $\left|\chi_2\right\rangle$ we have, by the same procedure,

$$\frac{\partial}{\partial x}\left|\chi_2\right\rangle = \begin{pmatrix}e^{i\phi}\cos(\gamma)\cos(\theta)\frac{\partial\theta}{\partial x} - \sin(\gamma)\sin(\theta)\frac{\partial\gamma}{\partial x}e^{i\phi} + e^{i\phi}i\cos(\gamma)\frac{\partial\phi}{\partial x}\sin(\theta) \\ \cos(\gamma)\frac{\partial\theta}{\partial x}(-\sin(\theta)) - \cos(\theta)\frac{\partial\gamma}{\partial x}\sin(\gamma) \\ -\cos(\gamma)\frac{\partial\gamma}{\partial x}\end{pmatrix},$$

and similar for $\frac{\partial}{\partial y}$ and $\frac{\partial}{\partial z}$. With this we calculate

$$\vec{A}_{22} = i\hbar\left\langle\chi_2|\vec{\nabla}\chi_2\right\rangle = i\hbar\begin{pmatrix}\left\langle\chi_2|\vec{\nabla}\chi_2\right\rangle_x \\ \left\langle\chi_2|\vec{\nabla}\chi_2\right\rangle_y \\ \left\langle\chi_2|\vec{\nabla}\chi_2\right\rangle_z\end{pmatrix},\tag{25}$$

with components

$$\begin{aligned}\left\langle\chi_2|\vec{\nabla}\chi_2\right\rangle_x =& i\frac{\partial\phi}{\partial x}\sin^2(\theta)\cos^2(\gamma) - \cos(\theta)\sin(\theta)\frac{\partial\theta}{\partial x}\cos^2(\gamma) \\ &+ \cos(\theta)\frac{\partial\theta}{\partial x}\sin(\theta)\cos^2(\gamma) - \frac{\partial\gamma}{\partial x}\sin(\gamma)\sin^2(\theta)\cos(\gamma) \\ &- \cos^2(\theta)\sin(\gamma)\frac{\partial\gamma}{\partial x}\cos(\gamma) + \frac{\partial\gamma}{\partial x}\sin(\gamma)\cos(\gamma) \\ =& i\frac{\partial\phi}{\partial x}\sin^2(\theta)\cos^2(\gamma),\end{aligned}\tag{26}$$

and thus we have for the vector potential

$$\vec{A}_{22} = -\hbar\sin^2(\theta)\cos^2(\gamma)\vec{\nabla}\phi \approx -\hbar\sin^2(\theta)\vec{\nabla}\phi,\tag{27}$$

because $\cos^2(\gamma) \approx 1$ when $\Delta \gg \Omega$. So indeed the opposite spins have opposite vector potential and therefore opposite magnetic field.

For the magnetic field we have:

$$
\vec{B} = \vec{\nabla} \times \vec{A} = \vec{\nabla} \times (\pm\hbar\sin^2(\theta)\vec{\nabla}\phi)
$$

$$
= \pm 2\hbar\sin(\theta)\cos(\theta)\begin{pmatrix} \frac{\partial\theta}{\partial y}\frac{\partial\phi}{\partial z} - \frac{\partial\theta}{\partial z}\frac{\partial\phi}{\partial y} \\ \frac{\partial\theta}{\partial z}\frac{\partial\phi}{\partial x} - \frac{\partial\theta}{\partial x}\frac{\partial\phi}{\partial z} \\ \frac{\partial\theta}{\partial x}\frac{\partial\phi}{\partial y} - \frac{\partial\theta}{\partial y}\frac{\partial\phi}{\partial x} \end{pmatrix}
$$

$$
= \pm\hbar\sin(2\theta)(\vec{\nabla}\theta \times \vec{\nabla}\phi), \tag{28}
$$

where we used $\frac{\partial^2\phi}{\partial x\partial y} - \frac{\partial^2\phi}{\partial y\partial x} = 0$ in the third step. This expression for $\vec{B}$ shows that there needs to be a gradient in both θ and ϕ and that these gradients should not be collinear if we want a nonzero magnetic field. The gradient in ϕ implies a gradient in the phase of the laser beams. The gradient in θ implies a gradient in the intensity ratio. According to the article of Dalibard *et al.*[9], the gradient in θ can also be a gradient in detuning from resonance. Notice also that $\vec{B}$ is independent of the intensity of the laser light, showing that the pseudo magnetic field is a geometric effect and the intensity just has to be large enough to satisfy the adiabatic condition.

When we rewrite equation 28 in terms of $\tan(\theta) = \frac{|\Omega_1|}{|\Omega_2|}$, so that it is written in terms of the intensity ratio and phase difference, we get the following equation for $\vec{B}$:

$$
\vec{B} = \frac{\hbar}{2}\vec{\nabla}\left(\frac{1 - \tan^2(\theta)}{1 + \tan^2(\theta)}\right) \times \vec{\nabla}\phi = \frac{\hbar}{2}\vec{\nabla}\left(\frac{1 - \frac{|\Omega_1|^2}{|\Omega_2|}}{1 + \frac{|\Omega_1|^2}{|\Omega_2|}}\right) \times \vec{\nabla}\phi \tag{29}
$$

3 Experimental implementation

In this section we discuss the experimental implementation of the light-induced magnetic field. We choose a laser configuration and for this we determine suitable parameters.

3.1 Laser configuration

For our actual experiment, we want to use the proposal in the articles of Dalibard *et al.*[9] and Zhu *et al.*[10] of two Gaussian counter-propagating laser beams which are spatially shifted. This is represented in figure 9. In the Rabi frequencies for these beams we take $k_1 = k_2 = k$, because they are almost equal; the energy difference between the ground states is negligible compared to the energy difference with the excited state, and the detuning is still relatively small. We also neglect deflection along the x-axis. The profile of the laser beams then becomes

$$\Omega_1 = \Omega_0 \exp\left(\frac{-(x-a)^2}{w^2}\right)\exp(-iky),$$
$$\Omega_2 = \Omega_0 \exp\left(\frac{-(x+a)^2}{w^2}\right)\exp(iky), \tag{30}$$

where a is the displacement of the laser beams from the centre and w is the waist of the laser beam profile, which we take equal for both lasers. With this, the phase difference $\phi = 2ky$, $\Omega\sin(\theta) = \Omega_0\exp(\frac{-(x-a)^2}{w^2})$ and $\Omega\cos(\theta) = \Omega_0\exp(\frac{-(x+a)^2}{w^2})$, so that

$$\tan(\theta) = \frac{\exp(\frac{-(x-a)^2}{w^2})}{\exp(\frac{-(x+a)^2}{w^2})} = \exp\left(\frac{4ax}{w^2}\right). \tag{31}$$

With this we have the following equations for $\vec{A}$ and $\vec{B}$:

$$\vec{A} = \pm\hbar\sin^2(\theta)\vec{\nabla}\phi = \pm\hbar(\frac{\tan(\theta)}{\sqrt{1+\tan^2(\theta)}})^2 \cdot 2k\hat{y} = \pm\frac{2k\hbar}{1+\exp(\frac{-8ax}{w^2})}\hat{y} \quad (32)$$

$$\vec{B} = \vec{\nabla}\times\vec{A} = \pm\frac{16\hbar ka}{w^2}\frac{\exp(\frac{-8ax}{w^2})}{(1+\exp(\frac{-8ax}{w^2}))^2}\hat{z} = \pm\frac{4\hbar ka}{w^2}\frac{1}{\cosh^2(\frac{4ax}{w^2})}\hat{z}. \tag{33}$$
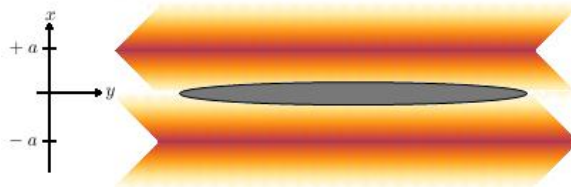

Figure 9: Setup for the laser beams. Two Gaussian counter-propagating laser beams, which are spatially shifted by a distance a from the y-axes, and in the middle the cloud of atoms.

3.2 Conditions

If we want $|\chi_2\rangle$ to have a negligible contribution of the excited state, so that we do not have to worry about heating from spontaneous emission, we need $\sin\gamma \approx 0$ and for this we need to have $\Delta \gg \Omega$ as we will now show. If $\Delta \gg \Omega$, we have

$$\lim_{\frac{\Omega}{\Delta}\to 0}\tan\gamma = \lim_{\frac{\Omega}{\Delta}\to 0}\frac{\sqrt{\Delta^2+\Omega^2}-\Delta}{\Omega} = \lim_{\zeta\to 0}\frac{\sqrt{1+\zeta^2}-1}{\zeta} = \lim_{\zeta\to 0}\frac{\frac{\zeta}{\sqrt{1+\zeta^2}}}{1} = 0, \quad (34)$$

where we used l'Hôpital's rule. Since $\tan\gamma \to 0$ implies $\sin\gamma \to 0$, $|\chi_2\rangle$ has a negligible contribution of the excited state when $\Delta \gg \Omega$. This gives the first condition.

According to the article of Zhu *et al.*[10], the adiabatic condition is:

$$\cos^2(\theta)|\vec{v}\cdot\vec{\nabla}(\tan(\theta)e^{i\phi})| \ll \frac{\Omega^2}{2\Delta}, \tag{35}$$

where $\vec{v}$ is the velocity of the atoms. This is commented on in appendix C. Worked out explicitly for our configuration it becomes

$$
\frac{1}{1+\tan^2(\theta)}|\vec{v}\cdot\vec{\nabla}(\tan(\theta)e^{i\phi})| = \frac{1}{1+\exp(\frac{8ax}{w^2})}|\vec{v}\cdot\vec{\nabla}(\exp(\frac{4ax}{w^2})e^{i2ky})|
$$
$$
= \frac{\exp(\frac{4ax}{w^2})}{1+\exp(\frac{8ax}{w^2})}|v_x\frac{4a}{w^2}+v_y 2ki|
$$
$$
= \frac{\sqrt{\frac{v_x^2 4a^2}{w^4}+v_y^2 k^2}}{\cosh(\frac{4ax}{w^2})} \ll \frac{\Omega^2}{2\Delta}. \tag{36}
$$

Now we use the definition of Ω from section 2.1,

$$
\Omega = \sqrt{|\Omega_1|^2+|\Omega_2|^2}
$$
$$
= \sqrt{\Omega_0^2(\exp(\frac{-2(x-a)^2}{w^2})+\exp(\frac{-2(x+a)^2}{w^2}))}
$$
$$
= \Omega_0 \exp(\frac{-x^2}{w^2})\exp(\frac{-a^2}{w^2})\sqrt{2\cosh(\frac{4ax}{w^2})} \tag{37}
$$

and the final expression for the adiabatic condition becomes:

$$\sqrt{\frac{v_x^2 4a^2}{w^4}+v_y^2 k^2} \ll \frac{\Omega_0^2}{\Delta}\exp(\frac{-2x^2}{w^2})\exp(\frac{-2a^2}{w^2})\cosh^2(\frac{4ax}{w^2}) = \alpha\frac{\Omega_0^2}{\Delta}. \tag{38}$$

From the condition we see that the newly defined adiabatic factor $\alpha = \exp(\frac{-2x^2}{w^2})\exp(\frac{-2a^2}{w^2})\cosh^2(\frac{4ax}{w^2})$ has to be large wherever you want the effect.

Now we take l as half the length over which we want the effect in the x-direction, so that the ends of this region are at $-l$ and at $+l$ and we write a, w and x in units of l, $a \to \bar{a}l$, $w \to \bar{w}l$ and $x \to \bar{x}l$, to get from equation 33:

$$B = \pm \frac{4\hbar k \bar{a}}{l \bar{w}^2} \frac{1}{\cosh^2(\frac{4\bar{x}\bar{a}}{\bar{w}^2})}. \tag{39}$$

The factor in the adiabatic condition (plotted in figure 10) becomes:

$$\alpha = \exp(\frac{-2\bar{x}^2}{\bar{w}^2}) \exp(\frac{-2\bar{a}^2}{\bar{w}^2}) \cosh^2(\frac{4\bar{a}\bar{x}}{\bar{w}^2}). \tag{40}$$
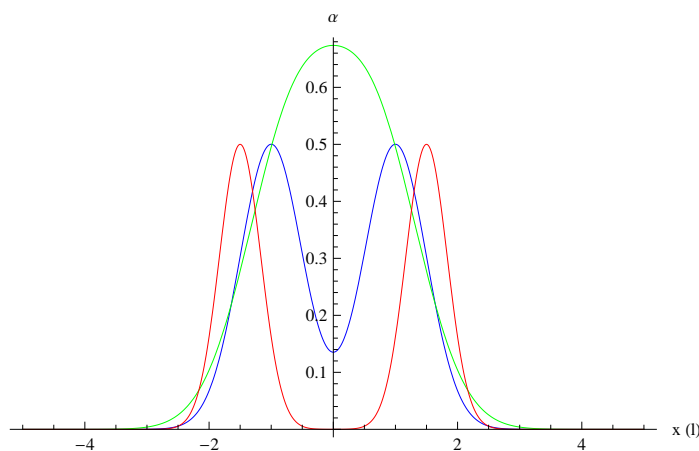
Figure 10: The factor in the adiabatic condition as a function of $\bar{x}$ for $\{\bar{a}, \bar{w}\} = \{\frac{2}{3}, \frac{3}{2}\}$ (green), $\{\bar{a}, \bar{w}\} = \{1, 1\}$ (blue) and $\{\bar{a}, \bar{w}\} = \{\frac{3}{2}, \frac{2}{3}\}$ (red). These are all qualitatively different shapes the adiabatic factor can take.

As can be seen from figure 10, the minimum for the adiabatic factor at the interval $(-l, +l)$ (where we want the effect), occurs at $\bar{x} = 0$ or at the boundary of this interval, so at $\bar{x} = 1$. Since we want the effect over the whole region, the bottleneck is where the adiabatic factor is minimum. Therefore we want this factor to be large both at $\bar{x} = 0$ and at $\bar{x} = 1$. In figure 11 is shown from what region we can choose $\bar{a}$ and $\bar{w}$ in order to have the adiabatic factor greater than 0.1 or 0.5 for the whole region. Which one is appropriate depends on how much the adiabatic condition can be satisfied by $\frac{\Omega_0^2}{\Delta}$, and the factor could possibly be even lower than 0.1. However, a more homogeneous satisfied adiabatic condition seems more natural and may also be better when considering heating effects, since we need less intensity.

For small $\bar{a}$, the laser beams are close to the centre and we can get a problem at $\bar{x} = 1$, and for large $\bar{a}$, the laser beams are far from the centre and we can get a problem at $\bar{x} = 0$. This can always be solved by increasing $\bar{w}$. These observations can also be seen in figure 11. We can also see from the figure which $\bar{a}$ we can use for a fixed $\bar{w}$ and still have a suitably large adiabatic factor. Notice that the spike follows about $\bar{a} = \frac{\bar{w}}{2}$, so this is a good choice to start from most of the time.
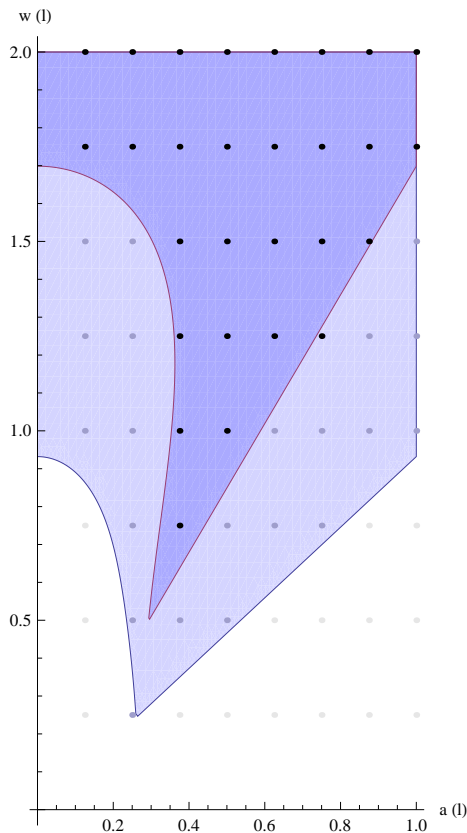
21

Figure 11: Regions in the $\bar{a}\bar{w}$-plane for which the adiabatic factor is greater than 0.1 (lighter blue) and for which it is greater than 0.5 (darker blue) everywhere on the interval $(-l, +l)$.

The expression for B in new units of l, equation 39, shows that the effect is inversely proportional to the system length l, and also that it only depends on $\bar{a}$ and $\bar{w}$ through the combination parameter $\frac{\bar{a}}{\bar{w}^2}$. This parameter, together with the system length l, completely determines the value and shape of B as a function of $\bar{x}$ for a given k. We now investigate what will be good choices for this parameter. When we choose it too large, the effect will only be large in a small region and when we choose it too small, the effect will be on a large length scale, but small everywhere. This is also illustrated by calculating the integral $\int_{-\infty}^{\infty} \frac{\alpha}{\cosh^2(4\alpha x)} \, dx = \int_{-\infty}^{\infty} \frac{1}{\cosh^2(4s)} \, ds = \frac{1}{2}$, which shows that we can only redistribute the area of the plot of B and not increase it, because this is independent of $\frac{\bar{a}}{\bar{w}^2}$. We thus search for a value of $\frac{\bar{a}}{\bar{w}^2}$ which distributes this in an optimal way. Since $\frac{\bar{a}}{\bar{w}^2}$ is the relevant parameter, in figure 12 we also plot the regions for which the adiabatic factor is greater than a certain value in the $\bar{w}^2\bar{a}$-plane. In this plane, the slope of the line between the origin and a point is equal to $\frac{\bar{a}}{\bar{w}^2}$, so we can easily see what $\bar{a}$ and $\bar{w}$ we can choose for a given $\frac{\bar{a}}{\bar{w}^2}$. This also shows the maximum value of $\frac{\bar{a}}{\bar{w}^2}$ we can achieve, keeping the adiabatic condition in mind. This is the maximum slope for which the line through the origin intersects with the colored region.
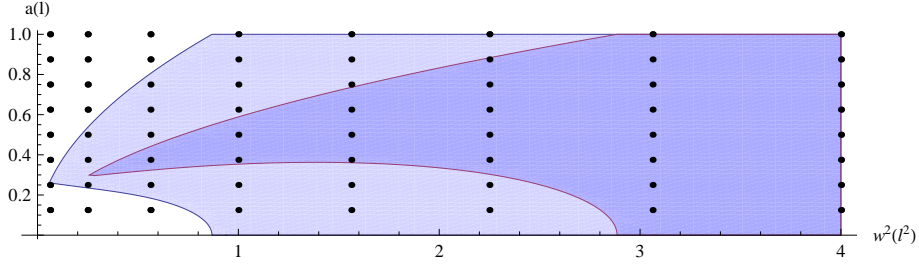
Figure 12: Regions in the $\bar{w}^2\bar{a}$-plane for which the adiabatic factor is greater than 0.1 (lighter blue) and for which it is greater than 0.5 (darker blue) everywhere on the interval $(-l, +l)$.

3.2.1 Homogeneous magnetic field

One possible condition we could impose in order to choose a value for $\frac{\bar{a}}{\bar{w}^2}$, is to demand that the magnetic field is homogeneous within a certain percentage. Since the expression for B has its maximum at $\bar{x} = 0$ and it monotonously decays when moving away from $\bar{x} = 0$, $B(\bar{x} = 0)$ and $B(\bar{x} = 1)$ differ the most. Since $\frac{1}{\cosh(0)} = 1$, we can set $\frac{1}{\cosh(\frac{4\bar{a}}{\bar{w}^2})} = f$ where f is the relative factor we allow. For a factor closer to 1, we need $\frac{\bar{a}}{\bar{w}^2}$ closer to zero. However, the greater $\frac{\bar{a}}{\bar{w}^2}$, the greater $B(\bar{x} = 0)$, thus here we need a compromise. When we want B to vary within 10 percent, we can take $\frac{1}{\cosh^2(\frac{1}{3})} \approx 0.90$, or when we want B to vary within 6 percent, we can take $\frac{1}{\cosh^2(\frac{1}{4})} \approx 0.94$. This fixes $\frac{4\bar{a}}{\bar{w}^2} = \frac{1}{3}$ or $\frac{4\bar{a}}{\bar{w}^2} = \frac{1}{4}$.

3.2.2 Maximum value of B at a certain value of $\bar{x}$

Another condition in order to find a value for $\frac{\bar{a}}{\bar{w}^2}$, is to demand that the value of B is optimal at a certain fixed nonzero $\bar{x}$. We write $B = \frac{4\hbar k\bar{a}}{l\bar{w}^2}\frac{1}{\cosh^2(\frac{4\bar{a}\bar{x}}{\bar{w}^2})} = \frac{\hbar k}{l\bar{x}}\frac{\gamma}{\cosh^2(\gamma)}$, with $\gamma = \frac{4\bar{a}\bar{x}}{\bar{w}^2}$, where $\bar{x}$ is a constant parameter. The function $\frac{\gamma}{\cosh^2(\gamma)}$ is plotted in figure 13, its maximum is at $\gamma \approx 0.772$ and it is largest for γ around this value. The condition for maximum B fixes $\frac{4\bar{a}\bar{x}}{\bar{w}^2} \approx 0.772$. Here $\bar{x}$ is the point at which we want the B-field as great as possible, so natural points would be for example $\bar{x} = 1$, at the boundary, or $\bar{x} = \frac{1}{2}$, which is at the middle from the centre.
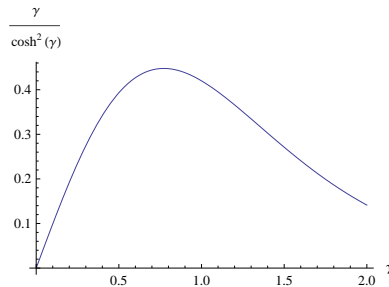

Figure 13: A plot of $\frac{\gamma}{\cosh^2(\gamma)}$.

23

3.3 Putting in the numbers

The relevant equations for the experiment, in which we want to put in real values, are the expression for B and the adiabatic condition, which we now restate:

$$B = \pm \frac{4\hbar k \bar{a}}{l\bar{w}^2} \frac{1}{\cosh^2(\frac{4\bar{x}\bar{a}}{\bar{w}^2})}. \tag{41}$$

$$\sqrt{\frac{v_x^2 4\bar{a}^2}{l^2\bar{w}^4} + v_y^2 k^2} \ll \alpha\frac{\Omega_0^2}{\Delta}. \tag{42}$$

In our experiment we use sodium atoms, which have a mass of $m = 3.816 \cdot 10^{-26}$ kg and we use laser light of wavelength λ_w of 589 nm, so that $k = \frac{2\pi}{\lambda_w} = 1.067 \cdot 10^7$ m^{-1}. For v_i, the speed we use in the adiabatic condition, we take

$$v = \frac{\hbar k_{\mathrm{dB}}}{m} = \frac{2\pi\hbar}{\lambda_{\mathrm{dB}}m} = \sqrt{\frac{2\pi k_{\mathrm{B}}T}{m}} \approx 47.7\sqrt{|T|}\,\frac{\mathrm{m}}{\mathrm{s}}, \tag{43}$$

where $\lambda_{\mathrm{dB}} = \hbar\sqrt{\frac{2\pi}{mk_{\mathrm{B}}T}}$ is the thermal de Broglie wavelength, T is the temperature, $k_{\mathrm{B}} = 1.38 \cdot 10^{-23}\,\frac{\mathrm{J}}{\mathrm{K}}$, the Boltzmann constant, and $\hbar = 1.05 \cdot 10^{-34}$ Js, the Planck constant.

For the intensity, we use the formula $s_0 = \frac{2|\Omega|^2}{\gamma^2}$, where $\gamma = 10$ MHz. When we set $\Delta = C_1\Omega_0$, where $C_1 \gg 1$ with the condition $\Delta \gg \Omega$ in mind, and set $C_2\sqrt{\frac{v_x^2 4\bar{a}^2}{l^2\bar{w}^4} + v_y^2 k^2} = \alpha\frac{\Omega_0^2}{\Delta}$ for the adiabatic condition, with $C_2 \gg 1$, we get $\Omega_0 = \frac{C_1 C_2}{\alpha}\sqrt{\frac{v_x^2 4\bar{a}^2}{l^2\bar{w}^4} + v_y^2 k^2}$. Now we can write the equation for s_0 at the centre of one laser beam as:

$$s_0 = \frac{2}{\gamma^2}\frac{C_1^2 C_2^2}{\alpha^2}\left(\frac{v_x^2 4\bar{a}^2}{l^2\bar{w}^4} + v_y^2 k^2\right) = \frac{C_1^2 C_2^2|T|}{\alpha^2}\left(\frac{1.82\cdot10^{-10}\bar{a}^2}{|l|^2\bar{w}^4} + 5.18\cdot10^3\right). \tag{44}$$

The factor $\frac{\bar{a}}{\bar{w}^2} < 1$ for almost all practical choices of $\bar{a}$ and $\bar{w}$, and for $|l| > 10^{-6}$ m, the first term in the brackets is negligible (the adiabatic condition is determined by the phase gradient of the laser and not by the gradient in intensity ratio) and we can write $s_0 \approx 5.18\cdot10^3\frac{C_1^2 C_2^2|T|}{\alpha^2}$.

3.3.1 Trial setup

In order to explore the experimental results we get from the chosen laser setup, we want to try some configurations which are easy to implement in our experiment. We will put our laser beams perpendicular to the long axes of our cigar shaped cloud of atoms, shown in figure 14. The effect is smaller than if we would put the lasers along the long axes, but probably it will be still large enough to measure effects. In our particular setup, the length scale l is 0.8 mm. We want to try $\bar{a} = 1$ and $\bar{w} \in \{1, 2, 4\}$.
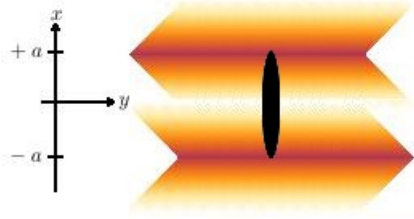
Figure 14: Trial setup for the laser beams, which is similar to figure 9.

From figure 11 we see that for $\bar{w} = 1$, we need to use the adiabatic factor $\alpha = 0.1$ and for the other two we can use $\alpha = 0.5$. The adiabatic condition then becomes $\frac{\Omega_0^2}{\Delta} \gg \frac{v_y k}{\alpha} = 5.01 \cdot 10^8 \frac{\sqrt{|T|}}{\alpha}$ Hz, where we have neglected the term with v_x, which is much smaller. We can use $T = 10^{-6}$ K, $\Delta = 10^9$ Hz and $\Omega_0 = 10^8$ Hz, so that the adiabatic condition is satisfied.

The value of B at $\bar{x} = 0$ becomes $B(\bar{x} = 0) = \frac{4\hbar k \bar{a}}{l \bar{w}^2} \approx 5.6 \cdot 10^{-24} \frac{1}{\bar{w}^2} \frac{\text{kg}}{\text{s}}$. In section 1 we plotted for $\frac{B}{m}$ and in this case we get $\frac{B}{m} \approx \frac{147}{\bar{w}^2}$ Hz. Although we used another aspect ratio for the trap, we can still use the results as approximation, because we get very similar shaped plots for ω for different cigar shaped traps. By comparing the value we found for $\frac{B}{m}$ with figure 1, we see that we can expect a noticeable change in the frequency when the effect would be homogeneous over the cloud. However, we have values $\frac{\bar{a}}{\bar{w}^2}$ out of $\{1, \frac{1}{4}, \frac{1}{16}\}$, and the effect at the boundary, $B(\bar{x} = 1)$ is a factor $\frac{1}{\cosh(\frac{4\bar{a}}{\bar{w}^2})} = \{0.001, 0.4, 0.94\}$ smaller. We see that the last is very homogeneous and the first is not. In figure 15 the value of $\frac{B}{m}$ is plotted for the $\bar{x} \in (-1, 1)$ for these different choices of $\bar{w}$.
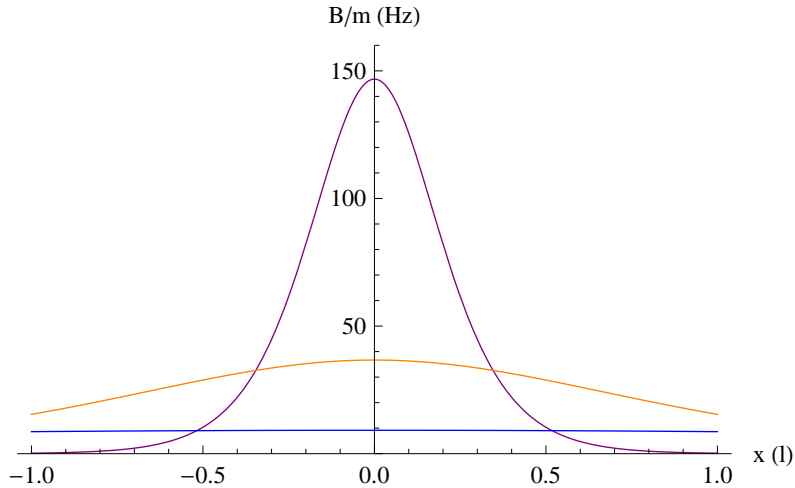

Figure 15: $\frac{B}{m}$ as a function of $\bar{x}$ for $\bar{w} = 1$ (red), $\bar{w} = 2$ (green) and $\bar{w} = 4$ (blue).

4 Discussion and Outlook

4.1 Discussion

We have shown the origin of the light-induced magnetic field and calculated the magnitude of the magnetic field for a realistic situation, for which we determined suitable parameters. From our phenomenological description, we expect this to give measurable effects in the experiment, so it is a good idea to investigate the effects further. However, there can be several side effects and it could be difficult to get the initial conditions right. Also, the adiabatic condition is not easily satisfied; we need slow atoms (low temperatures) and high intensities to make it work.

4.1.1 Theoretical improvements

Since the effect relies on the adiabatic approximation, the description of the adiabatic condition should be improved, possibly through perturbation theory, so that we can have more confidence in the theory. Also the extra potential effects should be analyzed in more detail. In section 1 we described the effects of a magnetic field by phenomenological equations. Here improvements can be made, for example by taking into account interactions between atoms and by using a quantum mechanical description. Effects could be calculated both for a thermal cloud and a Bose-Einstein condensate to see what differences we get. However, the main purpose of this thesis was to investigate experimental implementation of these light-induced magnetic fields and to verify that we can get measurable effects. The prospects for this are positive.

4.2 Outlook

When the setup of section 3.3.1 is implemented we can try to determine that it is indeed a Hall effect by showing that the displacement is opposite for opposite velocity of the cloud. For this we need a setup with large B in the middle, so we could choose $\bar{w} = 1$ or $\bar{w} = 2$. After this we could try to quantitatively measure the change in the collective mode frequency or the displacement r_a at $z = 0$, possibly as a function of B.

Another possibility is to try to use the effect multiple times by using multiple pairs of laser beams, created by putting a mask (a plate with holes in it) in front of a larger laser beam, to make a grid of laser beams. One of the drawbacks here is that you cannot add the B-fields, you have to go back to the intensity ratio in equation 29. The result is shown in figure 16. For large spacing between laser pairs, we have a change in sign of the B-field, when we go from one pair to another. This is because you can pair two lasers from different laser pairs and have a configuration opposite to the normal pairs, with large $\bar{a}$.

When the trial setup gives nice results, we can try to align the laser beams along the long axis of the cloud. This is a lot harder to implement in our experiment and proper alignment of the lasers is also a lot harder because the length scales are smaller and the alignment comes very precise. The B-field however, can be a lot higher, since the effects is inversely proportional to the system length l. Then we could choose to make a homogeneous B-field and by varying $\bar{a}$ and $\bar{w}$ we can choose the value for B within a fairly large region. We would also make optimal use of our cigar shaped trap, because we can have the large B-field for a relatively large system even though one direction is restricted to a small length scale.
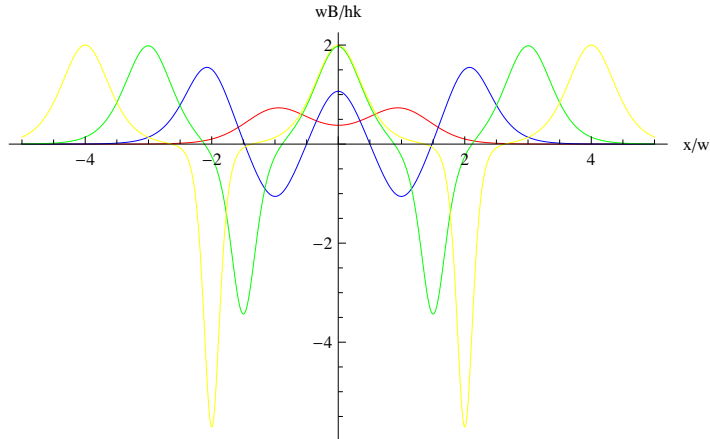

Figure 16: B as a function of x, for several pairs of laser beams. The dimensionless units are chosen this way for convenience. Here, for each laser pair, $a = \frac{w}{2}$ and the space between laser pairs is w (red), $2w$ (blue), $3w$(green) and $4w$ (yellow).

A Normal modes

In this appendix we examine the normal modes in detail. For the figures, we use the following values: $c = 1\,\text{Hz}$, $\omega_r = 100\,\frac{\text{rad}}{\text{s}}$, $\omega_z = 4\,\frac{\text{rad}}{\text{s}}$ and $a = 0$. We choose c this way, so that we can plot for $b = bc = \frac{B}{m}$ more easily, when c itself is not a relevant parameter and only comes in pairs with b, that is in a mode where there is no drag. When there is drag, we will plot for several values of c. Another way of looking at this is that we choose a new parameter $\frac{B}{m}$ for the modes without drag, and this parameter is what we use on our axes for all figures. We choose the ω this way, because they are relevant for our experiment. We choose a this way, because we are not hydrodynamic in the radial direction. Subsection A.5 is about the differences we get when a is not equal to zero. The modes are labeled according to the motion with $B = 0$, or equivalently $b = 0$. The first subsection is already included in the main text, but is mentioned here for completeness of this appendix.

A.1 In-phase oscillation in the z-direction

This mode starts from the mode in which both clouds oscillate in-phase in the z-direction. When we turn on the B-field, the clouds are separated in the r-direction, since the B-field acts oppositely on the clouds and their velocities are (approximately) in the same direction. Since there is no relative movement in the z-direction and there is no drag in the r-direction, there is no damping in this mode. In figure 17 the angular frequency is plotted against the B-field and in figure 18 the trajectory is plotted for $\frac{B}{m} = 100\,\text{Hz}$.
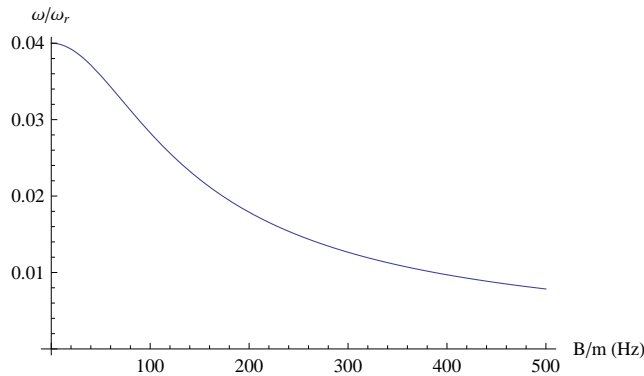

Figure 17: The angular frequency $\frac{\omega}{\omega_r}$ as a function of $\frac{B}{m}$ for the in-phase oscillation in the z-direction. Because there is no damping this quantity is completely real.
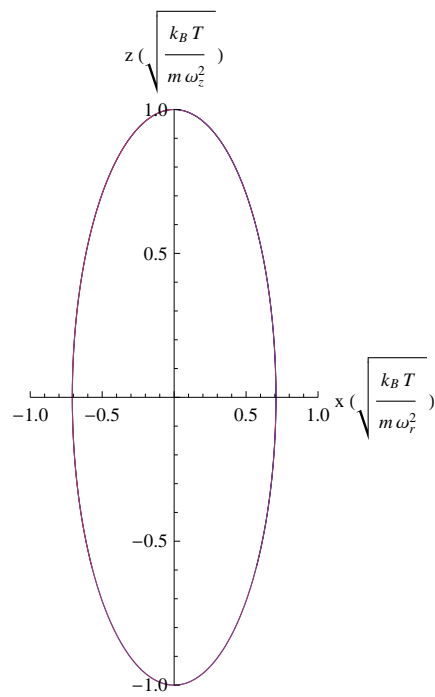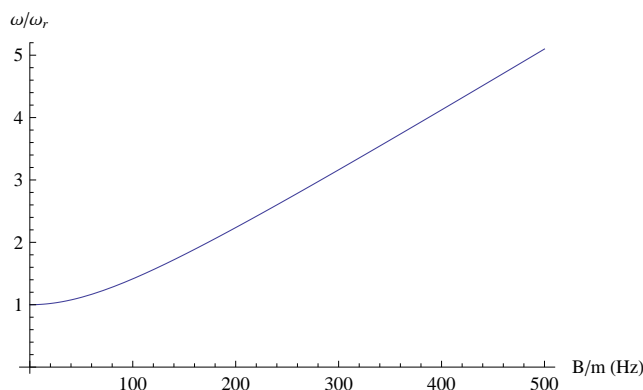
Figure 18: Trajectory of the normal mode starting from the in-phase oscillation in the z-direction. Note that we use different units on the axes. Here, $b = 100$, so $\frac{B}{m} = 100\,\text{Hz}$.

A.2 Out-of-phase oscillation in the r-direction

This mode starts from the mode in which the clouds oscillate out-of-phase in the r-direction, the spin dipole mode. When we turn on the B-field, the z-component of the force of this field is the same on both clouds, because both the velocity in the r-direction and the effect of B are opposite for the clouds. Because of that the clouds get the same speed in the z-direction. Since there is no drag in the r-direction and there is no relative speed in the z-direction, there is no damping in this mode. In figure 19 the angular frequency is plotted against the B-field and in figure 20 the trajectory is plotted for $\frac{B}{m} = 100\,\text{Hz}$.

Figure 19: The angular frequency $\frac{\omega}{\omega_r}$ as a function of $\frac{B}{m}$ for the out-of-phase oscillation in the r-direction. Because there is no damping this quantity is completely real.
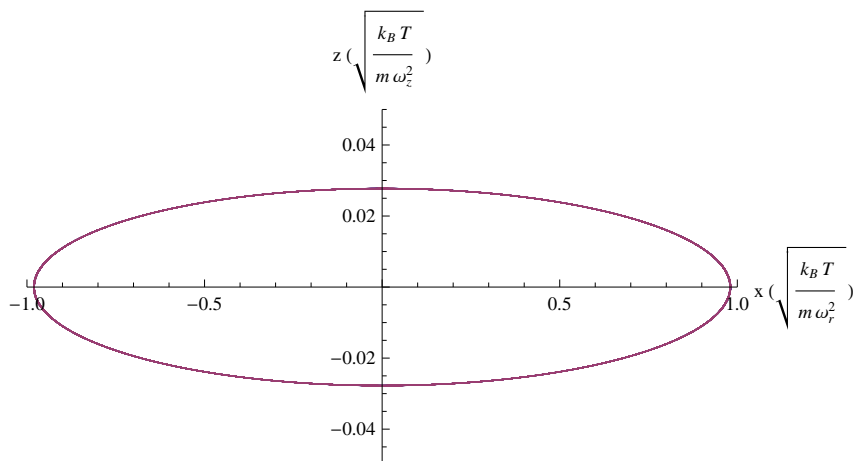

Figure 20: Trajectory of the normal mode starting from the out-of-phase oscillation in the r-direction. Note that we use different units on the axes. Here, $b = 100$, so $\frac{B}{m} = 100\,\text{Hz}$.

A.3 In-phase oscillation in the r-direction

This mode starts from the mode in which both clouds oscillate in-phase in the r-direction. When we turn on the B-field, the clouds are separated in the z-direction, since the B-field acts oppositely on the clouds and their speed in the r-direction is the same. The clouds get a relative speed in the z-direction and because of that there is damping in this mode. Therefore the value of c is important and we will plot for different c in the following figures. When B gets larger, the relative speed gets larger and because of that the damping gets larger. The amplitude is larger also. These observations can be seen by comparing figure 24 and figure 25, which have been plotted for the same amount of time. We also see that the frequency is a lot higher in figure 25 compared to figure 24, which is in agreement with figure 22.
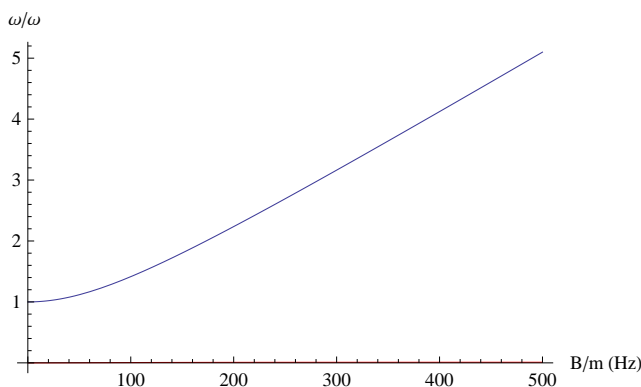

Figure 21: The angular frequency $\frac{\omega}{\omega_r}$ as a function of $\frac{B}{m}$ for the in-phase oscillation in the r-direction. Because there is damping this quantity has a real (blue) and an imaginary (red) part, which is hardly visible. In this figure, $c = 1\,\text{Hz}$.
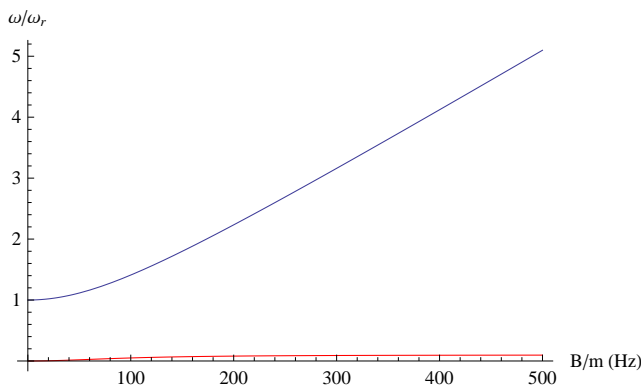

Figure 22: The angular frequency $\frac{\omega}{\omega_r}$ as a function of $\frac{B}{m}$ for the in-phase oscillation in the r-direction. Because there is damping this quantity has a real (blue) and an imaginary (red) part. In this figure, $c = 10\,\text{Hz}$.
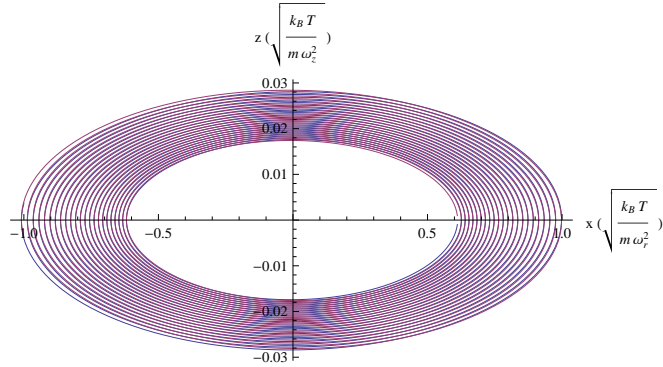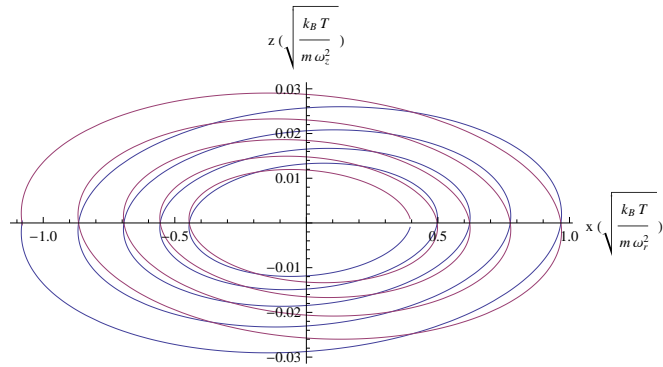
Figure 23: Trajectory of the normal mode starting from the in-phase oscillation in the r-direction. Note that we use different units on the axes. Here, $b = 100$ and $c = 1\,\text{Hz}$, so $\frac{B}{m} = bc = 100\,\text{Hz}$.

Figure 24: Trajectory of the normal mode starting from the in-phase oscillation in the r-direction. Note that we use different units on the axes. Here, $b = 10$ and $c = 10\,\text{Hz}$, so $\frac{B}{m} = bc = 100\,\text{Hz}$.
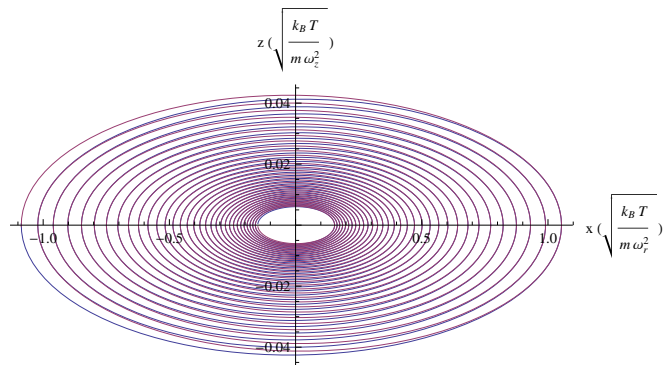

Figure 25: Trajectory of the normal mode starting from the in-phase oscillation in the r-direction. Note that we use different units on the axes. Here, $b = 100$ and $c = 10\,\text{Hz}$, so $\frac{B}{m} = bc = 1000\,\text{Hz}$.

A.4 Out-of-phase oscillation in the z-direction

This mode starts from the mode in which the clouds oscillate out-of-phase in the z-direction, the spin dipole mode. When we turn on the B-field, both clouds are moved in the r-direction. The force is the same, because the speed in the z-direction is opposite, as is the effect of the B-field. This mode is over-damped when c is too large, and in the experiment we expect it to be. When B is large enough, we may get to a point where the mode is not completely over-damped anymore. The B-field does not influence the absolute speed, but it does turn the velocity partially into the r-direction, in which there is no drag and because of which the speed in the z-direction gets smaller. Also the clouds are no longer in the minimum of the radial potential, and because of energy conservation, the clouds will have lower speed, and thus also lower relative speed. Because of this the damping gets less when B gets larger.
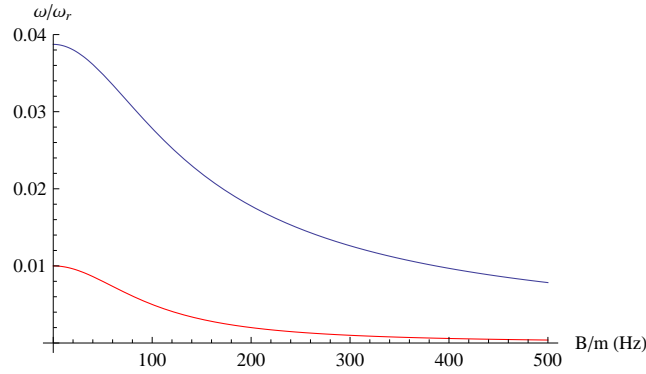

Figure 26: The angular frequency $\frac{\omega}{\omega_r}$ as a function of $\frac{B}{m}$ for the out-of-phase oscillation in the z-direction. Because there is damping this quantity has a real (blue) and an imaginary (red) part. In this figure, $c = 1\,\text{Hz}$.
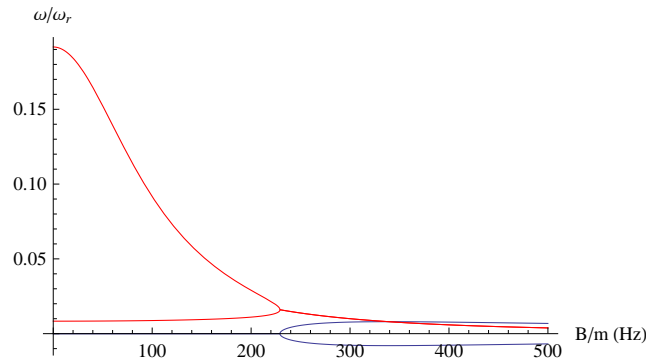

Figure 27: The angular frequency $\frac{\omega}{\omega_r}$ as a function of $\frac{B}{m}$ for the out-of-phase oscillation in the z-direction. Because there is damping this quantity has a real (blue) and an imaginary (red) part. In this figure, $c = 10\,\text{Hz}$.

Figure 28: Trajectory of the normal mode starting from the out-of-phase oscillation in the z-direction. Note that we use different units on the axes. Here, $b = 100$ and $c = 1\,\text{Hz}$, so $\frac{B}{m} = bc = 100\,\text{Hz}$.
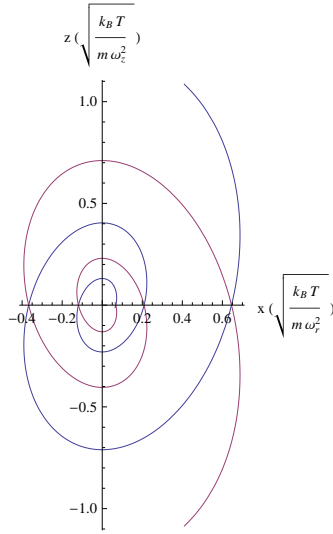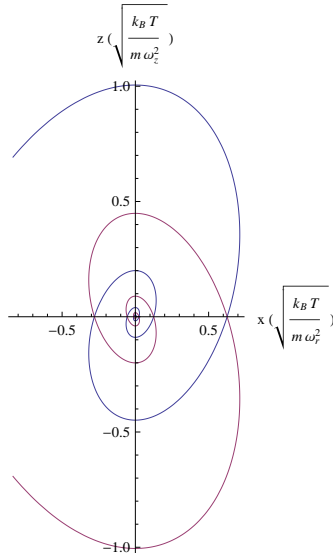

Figure 29: Trajectory of the normal mode starting from the out-of-phase oscillation in the z-direction. Note that we use different units on the axes. Here, $b = 100$ and $c = 10\,\text{Hz}$, so $\frac{B}{m} = bc = 1000\,\text{Hz}$.

For $b = 10$ and $c = 10\,\text{Hz}$, thus $\frac{B}{m} = bc = 100\,\text{Hz}$, the trajectory is over-damped and there is no point in plotting its trajectory. This and the plot of figure 29 are in agreement with figure 27, which shows a certain critical value for $\frac{B}{m}$ above which the trajectory is no longer over-damped.

34

A.5 Differences when there is also drag in the r-direction

When we choose $a = 1$ instead of $a = 0$, we have the same drag in both directions and now we consider the differences we get in comparison with the previous normal modes.

The in-phase oscillation in the r-direction and the out-of-phase oscillation in the z-direction do not have any relative motion in the r-direction and therefore the value of a has no influence on the trajectories.

In the in-phase oscillation in the z-direction, the speed in the r-direction is relatively small, and therefore also the relative speed is small. Because of this there is hardly any difference when we put $a = 1$ instead of $a = 0$. Only for the out-of-phase oscillation in the r-direction, there is a clear difference and this is because the relative movement in the r-direction is precisely the most important movement in this mode. The trajectory is still comparable, with the difference that the trajectory gets smaller every cycle, as is shown in figure 30.
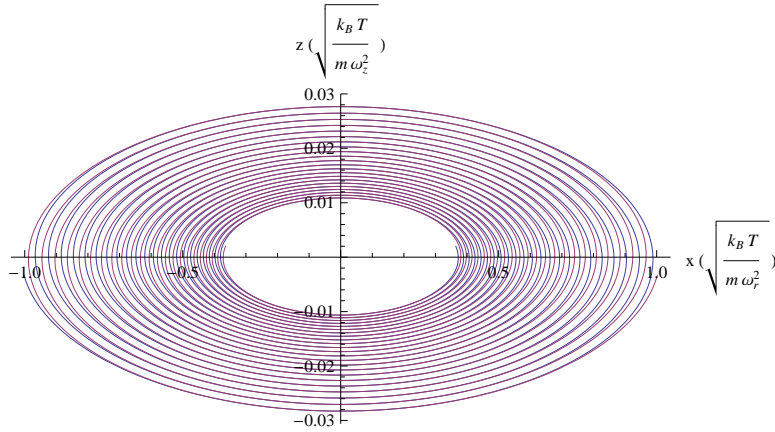

Figure 30: Trajectory of the normal mode starting from the out-of-phase oscillation in the r-direction. Note that we use different units on the axes. Here, $b = 100$, $c = 1\,\mathrm{Hz}$ and $a = 1$, so $\frac{B}{m} = bc = 100\,\mathrm{Hz}$.

B Eigenstates

In this appendix, we check that the states in section 2.1 are indeed eigenstates of $\hat{U}$:

$$\hat{U}\left|\chi_1\right\rangle = \begin{pmatrix} 0 & 0 & \Omega_1 \\ 0 & 0 & \Omega_2 \\ \Omega_1{}^* & \Omega_2{}^* & 2\Delta \end{pmatrix} \cdot \begin{pmatrix} \cos(\theta) \\ -\sin(\theta)e^{-i\phi} \\ 0 \end{pmatrix}$$

$$= \begin{pmatrix} 0 \\ 0 \\ \Omega\sin(\theta)e^{-i\phi}\cos(\theta) - \Omega\cos(\theta)\sin(\theta)e^{-i\phi} \end{pmatrix} = \begin{pmatrix} 0 \\ 0 \\ 0 \end{pmatrix}. \quad (45)$$

$$\hat{U}\left|\chi_2\right\rangle = \begin{pmatrix} 0 & 0 & \Omega_1 \\ 0 & 0 & \Omega_2 \\ \Omega_1{}^* & \Omega_2{}^* & 2\Delta \end{pmatrix} \cdot \begin{pmatrix} \sin(\theta)\cos(\gamma)e^{i\phi} \\ \cos(\theta)\cos(\gamma) \\ -\sin(\gamma) \end{pmatrix}$$

$$= \cos(\gamma) \begin{pmatrix} \Omega\sin(\theta)e^{i\phi}\frac{\Delta - \sqrt{\Delta^2+\Omega^2}}{\Omega} \\ \Omega\cos(\theta)\frac{\Delta - \sqrt{\Delta^2+\Omega^2}}{\Omega} \\ \Omega\sin^2(\theta) + \Omega\cos^2(\theta) + 2\Delta\frac{\Delta-\sqrt{\Delta^2+\Omega^2}}{\Omega} \end{pmatrix}$$

$$= \begin{pmatrix} \cos(\gamma)\sin(\theta)e^{i\phi}(\Delta - \sqrt{\Delta^2+\Omega^2}) \\ \cos(\gamma)\cos(\theta)(\Delta - \sqrt{\Delta^2+\Omega^2}) \\ \cos(\gamma)\frac{\Delta-\sqrt{\Delta^2+\Omega^2}}{\Omega}(\Delta - \sqrt{\Delta^2+\Omega^2}) \end{pmatrix}$$

$$= (\Delta - \sqrt{\Delta^2+\Omega^2})\left|\chi_2\right\rangle. \quad (46)$$

$$\hat{U}\left|\chi_3\right\rangle = \begin{pmatrix} 0 & 0 & \Omega_1 \\ 0 & 0 & \Omega_2 \\ \Omega_1{}^* & \Omega_2{}^* & 2\Delta \end{pmatrix} \cdot \begin{pmatrix} \sin(\theta)\sin(\gamma)e^{i\phi} \\ \cos(\theta)\sin(\gamma) \\ \cos(\gamma) \end{pmatrix}$$

$$= \Omega\cos(\gamma) \begin{pmatrix} \sin(\theta)e^{i\phi} \\ \cos(\theta) \\ \sin^2(\theta)\frac{\sqrt{\Delta^2+\Omega^2}-\Delta}{\Omega} + \cos^2(\theta)\frac{\sqrt{\Delta^2+\Omega^2}-\Delta}{\Omega} + \frac{2\Delta}{\Omega} \end{pmatrix}$$

$$= (\Delta + \sqrt{\Delta^2+\Omega^2})\left|\chi_3\right\rangle. \quad (47)$$

where we used $\sin(\gamma) = \cos(\gamma)\tan(\gamma) = \cos(\gamma)\frac{\sqrt{\Delta^2+\Omega^2}-\Delta}{\Omega}$ and in the final step $\frac{\Omega}{\tan(\gamma)} = \frac{\Omega^2}{\sqrt{\Delta^2+\Omega^2}-\Delta} = \Delta + \sqrt{\Delta^2+\Omega^2}$.

C Potential and adiabatic condition

In this appendix, we work out $V^* = \sum_{j\neq l} \frac{\vec{A}_{lj}\vec{A}_{jl}}{2m} + V + \hbar\lambda_l$ more explicitly. By explicit calculation, using the definition $\vec{A}_{jl} = i\hbar \langle \chi_j|\vec{\nabla}\chi_l\rangle$, we can show that the following equations for $\vec{A}_{jl}$ hold:

$$\vec{A}_{12} = \vec{A}_{21}^* = \hbar\cos(\gamma)e^{i\phi}(i\vec{\nabla}\theta - \sin(\theta)\cos(\theta)\vec{\nabla}\phi), \tag{48}$$

$$\vec{A}_{13} = \vec{A}_{31}^* = \hbar\sin(\gamma)e^{i\phi}(i\vec{\nabla}\theta - \sin(\theta)\cos(\theta)\vec{\nabla}\phi), \tag{49}$$

$$\vec{A}_{23} = \vec{A}_{32}^* = -\hbar\sin^2(\theta)\sin(\gamma)\cos(\gamma)\vec{\nabla}\phi + i\hbar\vec{\nabla}\gamma. \tag{50}$$

With this we can show that the terms in $\sum_{j\neq l} \frac{\vec{A}_{lj}\vec{A}_{jl}}{2m}$ are the following:

$$\frac{\vec{A}_{12}\vec{A}_{21}}{2m} = \frac{|\vec{A}_{12}|^2}{2m} = \frac{\hbar^2\cos^2(\gamma)}{2m}(|\vec{\nabla}\theta|^2 + \sin^2(\theta)\cos^2(\theta)|\vec{\nabla}\phi|^2), \tag{51}$$

$$\frac{\vec{A}_{13}\vec{A}_{31}}{2m} = \frac{|\vec{A}_{13}|^2}{2m} = \frac{\hbar^2\sin^2(\gamma)}{2m}(|\vec{\nabla}\theta|^2 + \sin^2(\theta)\cos^2(\theta)|\vec{\nabla}\phi|^2), \tag{52}$$

$$\frac{\vec{A}_{23}\vec{A}_{32}}{2m} = \frac{|\vec{A}_{23}|^2}{2m} = \frac{\hbar^2}{2m}(\sin^4(\theta)\sin^2(\gamma)\cos^2(\gamma)|\vec{\nabla}\phi|^2 + |\vec{\nabla}\gamma|^2). \tag{53}$$

C.1 Adiabatic condition

We are only interested in $|\chi_1\rangle$ and $|\chi_2\rangle$, and for these the eigenvalues λ_i are 0 and $\Delta - \sqrt{\Delta^2 + \Omega^2}$ respectively. Since $\Delta \gg \Omega$, we can expand λ_2 as $\lambda_2 = \Delta(1 - \sqrt{1 + (\frac{\Omega}{\Delta})^2}) \approx -\frac{\Omega^2}{2\Delta}$. The adiabatic condition according to Zhu et al.[10], equation 35, is based on the condition that the off-diagonal elements in the Hamiltonian are much smaller than the difference of the eigenvalue contributions, which are in the potential V^*: $\hbar\lambda_1$ and $\hbar\lambda_1$. The off-diagonal elements in the Hamiltonian are the off-diagonal elements of $\hat{P}^2$ divided by $2m$. When we explicitly calculate the diagonal element $\hat{P}_{21}$, we get:

$$\hat{P}_{21} = -\vec{A}_{21}(P - \vec{A}_{11}) - (P - \vec{A}_{22})\vec{A}_{21} + \vec{A}_{23}\vec{A}_{31}$$
$$= -(\vec{A}_{21}P + P\vec{A}_{21}) + (\vec{A}_{21}\vec{A}_{11} + \vec{A}_{22}\vec{A}_{21} + \vec{A}_{23}\vec{A}_{31}) \tag{54}$$

And, using above expressions for $\vec{A}_{jl}$:

$$(\vec{A}_{21}\vec{A}_{11} + \vec{A}_{22}\vec{A}_{21} + \vec{A}_{23}\vec{A}_{31}) = \hbar^2 e^{-i\phi}\sin(\gamma)(\vec{\nabla}\theta - i\cos(\theta)\sin(\theta)\vec{\nabla}\phi)\cdot\vec{\nabla}\gamma \tag{55}$$

When we work out the left hand side of the adiabatic condition of equation 35, making a convenient choice for the phase inside the absolute value and comparing with $\vec{A}_{12}$ above, we get

$$\cos^2(\theta)|\vec{v}\cdot\vec{\nabla}(\tan(\theta)e^{i\phi})| = |\vec{v}\cdot(-\sin(\theta)\cos(\theta)\vec{\nabla}\phi + i\vec{\nabla}\theta)| = |\frac{\vec{p}}{m}\cdot\frac{\vec{A}_{12}}{\hbar\cos(\gamma)}| \tag{56}$$

When we approximate $\sin(\gamma) = 0$ and $\cos(\gamma) = 1$ (see the beginning of section 3.2), we can compare equation 54 (keeping in mind that $\vec{A}_{12} = \vec{A}_{21}^*$ and $\hat{P}_{21} = \hat{P}_{12}^*$, since it is Hermitian) with equation 55 and equation 56, and see that it is plausible for the adiabatic condition to look like this.

References

[1] H. Ritsch, P. Domokos, F Brennecke and T. Esslinger, *Cold atoms in cavity-generated dynamical optical potentials*, Rev. Mod. Phys. **85**, 553-601 (2013).

[2] J. Weiner, V.S. Bagnato, S. Zilio and P.S. Julienne, *Experiments and theory in cold and ultracold collisions*, Rev. Mod. Phys. **71**, 1-85 (1999).

[3] R.A. Duine and H.T.C Stoof, *Spin Drag in Noncondensed Bose Gases*, Phys. Rev. Lett. **103**, 170401 (2009).

[4] M. Polini and G. Vignale, *Spins in cold atoms - what a drag!*, Physics **2**, 87 (2009).

[5] V. Galitski and I.B. Spielman, *Spin-orbit coupling in quantum gases*, Nature **494** 49-54 (2013).

[6] E. van der Bijl and R.A. Duine, *Anomalous Hall conductivity from the dipole mode of spin-orbit-coupled cold-atom systems*, `arXiv:1107.0578 [cond-mat.quant-gas]` (2011).

[7] H.J. van Driel, R.A. Duine, and H.T.C. Stoof, *Spin drag Hall effect in a rotating Bose mixture*, `arXiv:1007.1088 [cond-mat.quant-gas]` (2010).

[8] D.A. Abanin, R.V. Gorbachev, K.S. Novoselov, A.K. Geim, and L.S. Levitov, *Giant Spin-Hall Effect Induced by the Zeeman Interaction in Graphene*, Phys. Rev. Lett. **107**, 096601 (2011).

[9] J. Dalibard, F. Gerbier, G. Juzeliunas and P. Öhberg, *Artificial gauge potentials for neutral atoms*, `arXiv:1008.5378 [cond-mat.quant-gas]` (2011).

[10] Zhu, S.-L., H. Fu, C.-J. Wu, S.-C. Zhang, and L.-M. Duan, *Spin Hall Effects for Cold Atoms in a Light-Induced Gauge Potential*, Phys. Rev. Lett. **97**, 240401 (2006).

[11] S.B. Koller, *Experiments on hydrodynamic transport in ultra-cold Bose gases*, Ph.D. thesis, University of Utrecht, The Netherlands (2012).